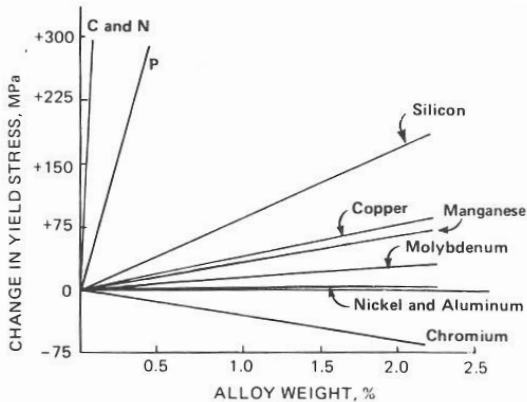
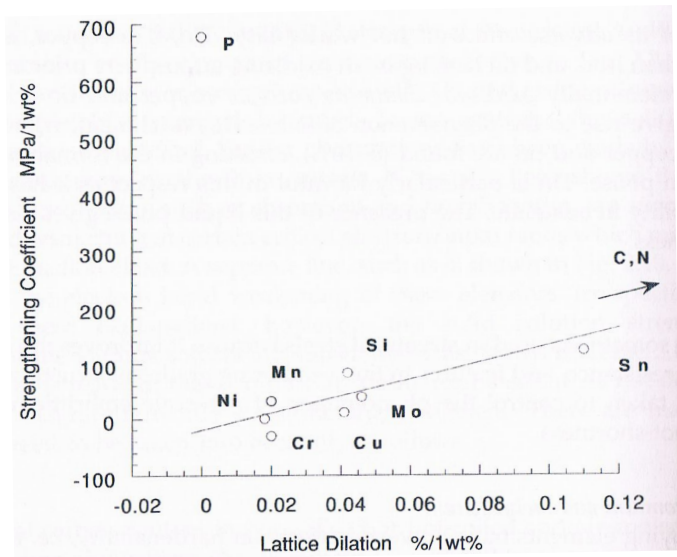


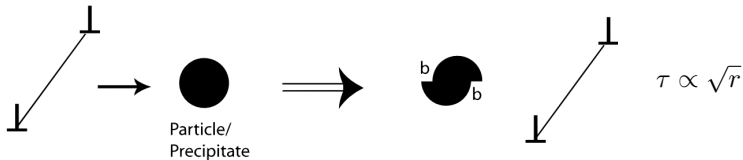
Solid solution strengthening



Solid solution strengthening effects in ferrite-pearlite high-strength low-alloy steels.



Particle strengthening



Coherency hardening

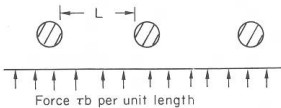
Surface hardening

Order hardening

Stacking fault hardening

Modulus hardening

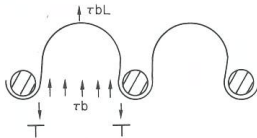
(a) Approach situation



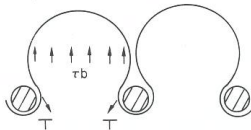
(b) Sub-critical situation



(c) Critical situation



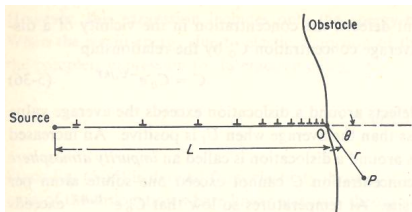
(d) Escape situation



Orowan equation

$$\tau = \frac{2T}{bL} \approx \frac{\mu b}{L}$$

Grain boundary strengthening



$$\text{Number of dislocations in pile up: } n \approx \frac{\tau_0 L}{\mu b}$$

$$\text{Normal stress acting across } OP: \sigma = \frac{3}{2} \left(\frac{L}{r} \right)^{\frac{1}{2}} \tau_0 \cos \frac{1}{2} \theta \sin \theta$$

$$\text{Shear stress acting on } OP: \tau = - \left(\frac{L}{4r} \right)^{\frac{1}{2}} \tau_0 \left(2 \cos \frac{1}{2} \theta - \sin \theta \sin \frac{3}{2} \theta \right)$$

Hall-Petch equation

I apply an additional shear stress, τ , to the pile-up and the resistance due to the GB is $(\tau - \tau_i)$. τ_i is the friction stress. Maximum stress in the next grain (Stroh) is

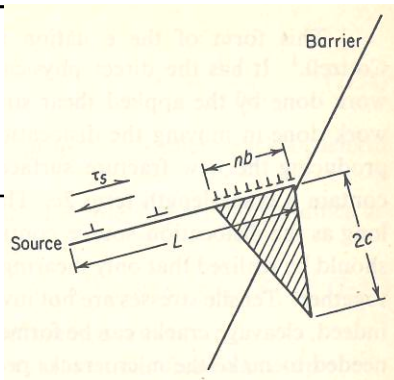
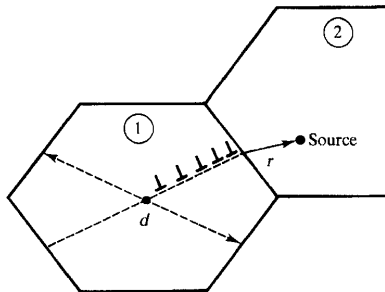
$$\tau_{\max} = (\tau - \tau_i)\sqrt{L/4r} \quad (1)$$

When τ reaches the shear stress in yielding, τ_y , sources are activated in the next grain. So (1) becomes

$$\tau_y = \tau_i + (\tau_{\max} \times 2\sqrt{r}) L^{-\frac{1}{2}}$$

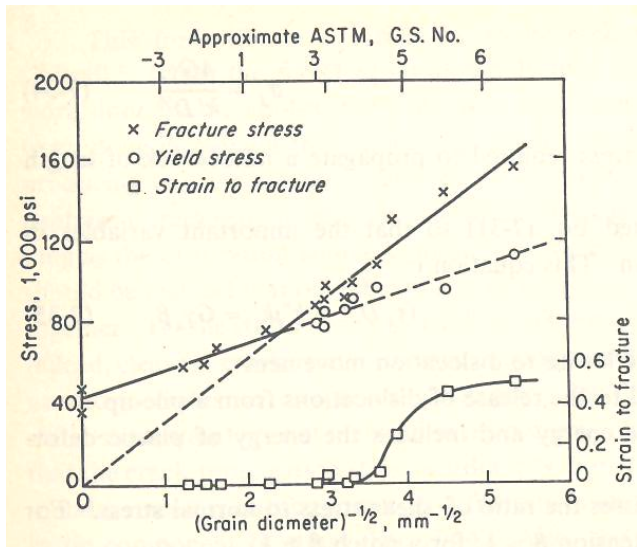
I can identify L with the grain size, d ; and after converting to tensile stress I get the Hall-Petch equation,

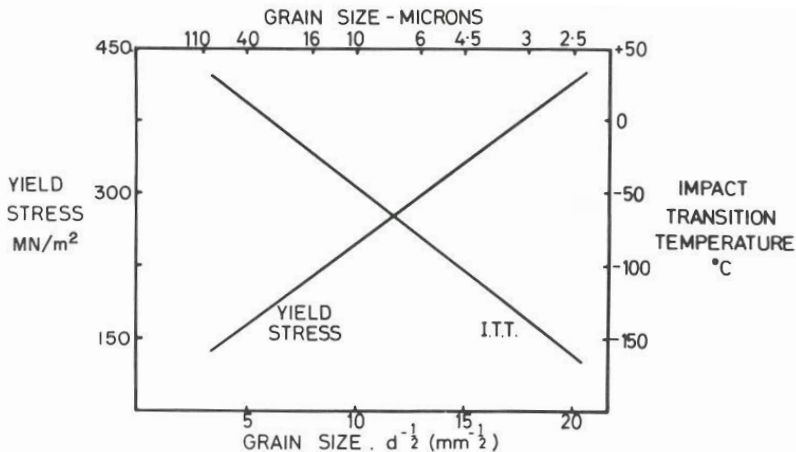
$$\sigma_y = \sigma_i + k_y d^{-\frac{1}{2}}$$



$$\sigma_y = \sigma_i + k_y d^{-\frac{1}{2}} \quad (\text{Hall-Petch equation})$$

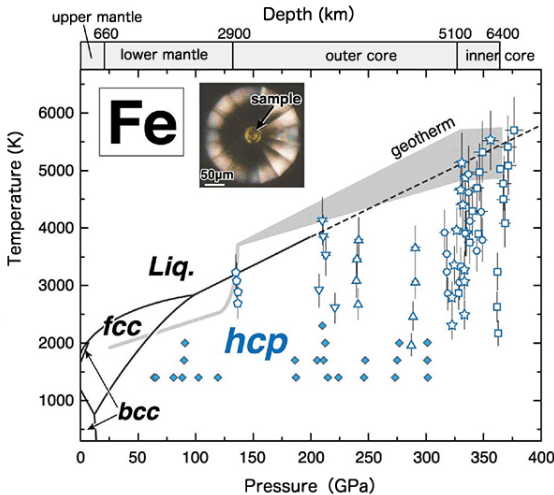
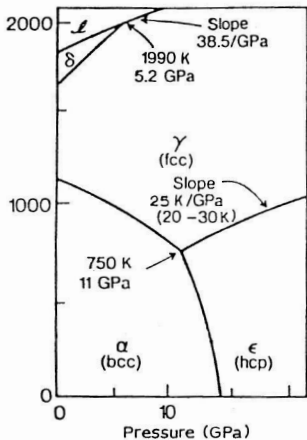
$$(\tau_s - \tau_i)nb \approx 2\gamma_s \longrightarrow \sigma_f \approx \frac{4\mu\gamma_s}{k_y} d^{-\frac{1}{2}} \quad (\text{Cottrell-Petch equation})$$

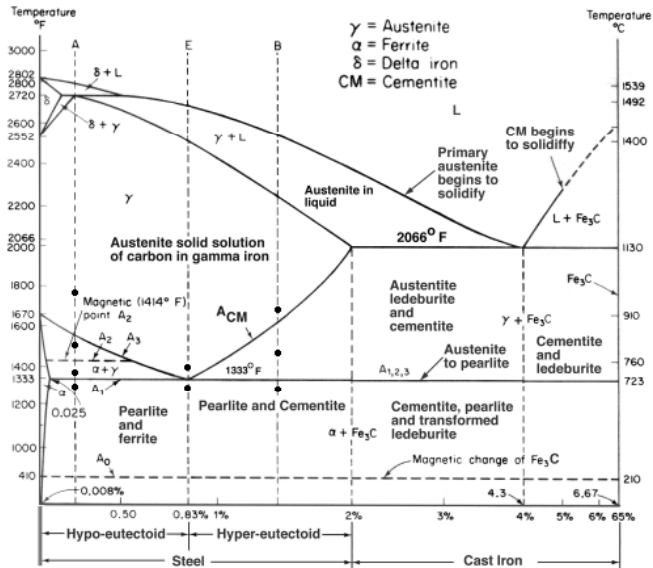
Low carbon steel at -196°C

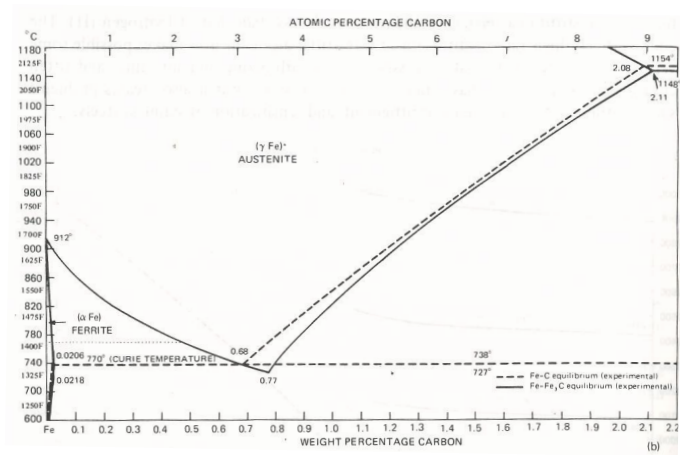


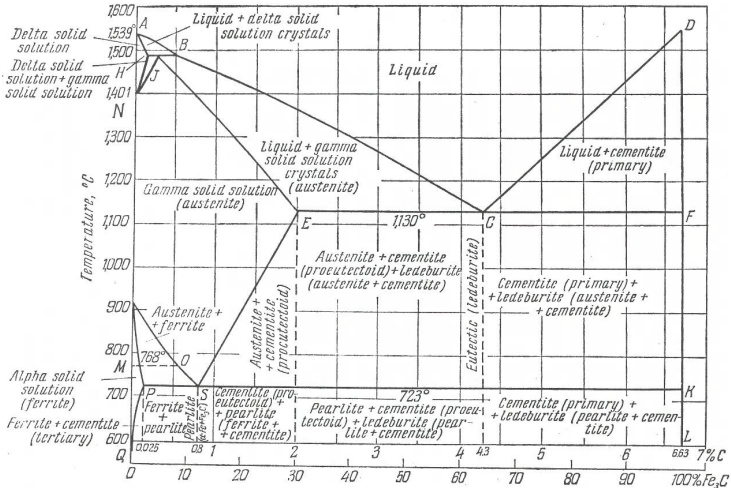
2.3. *Effect of grain size of ferrite on yield stress and impact transition temperature. (0.10% C; 0.50% Mn; 0.2% Si; 0.006% N).*

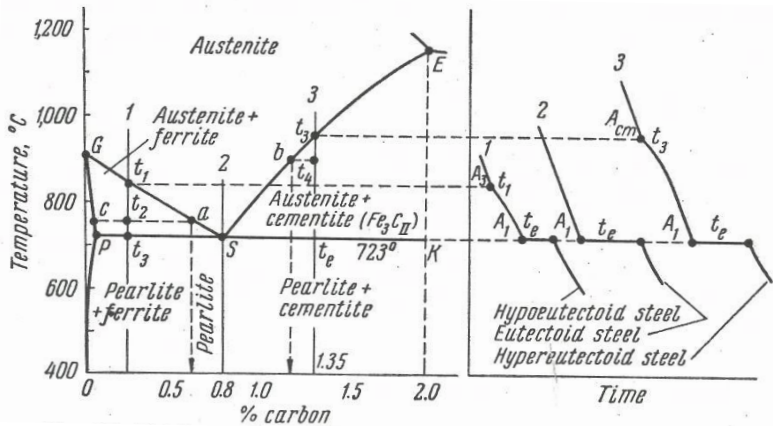
The Fe–C phase diagram

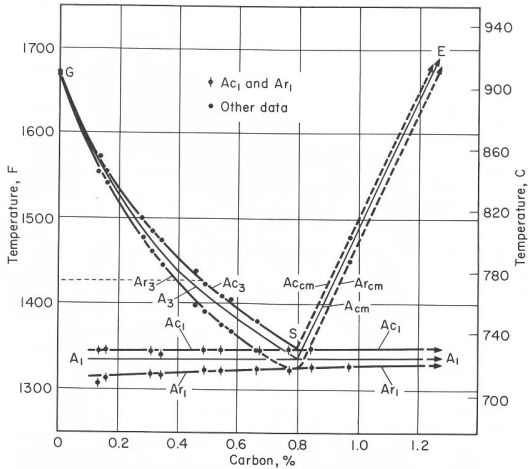












Cooling / heating at 0.125°C per minute

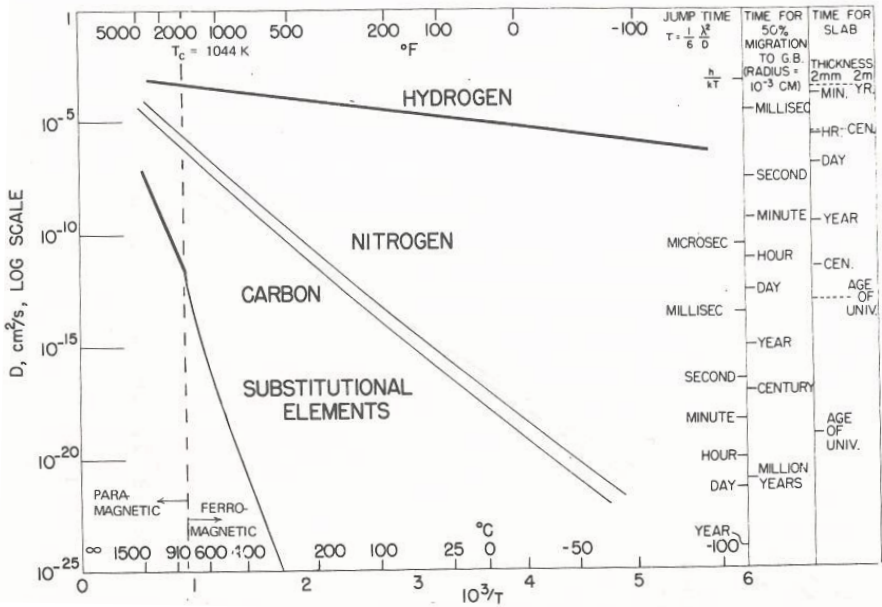
	<i>Change on heating</i>	<i>Change on cooling</i>
A_1	Pearlite to austenite	Austenite to pearlite
A_2	Loss of ferromagnetism	Gain of ferromagnetism
A_3	Last ferrite absorbed in austenite	First ferrite nucleates from austenite
A_{cm}	Last cementite absorbed in austenite	First cementite nucleates from austenite
A_4	First δ -iron forms from austenite	Last δ -iron dissolves in austenite

Diffusivity

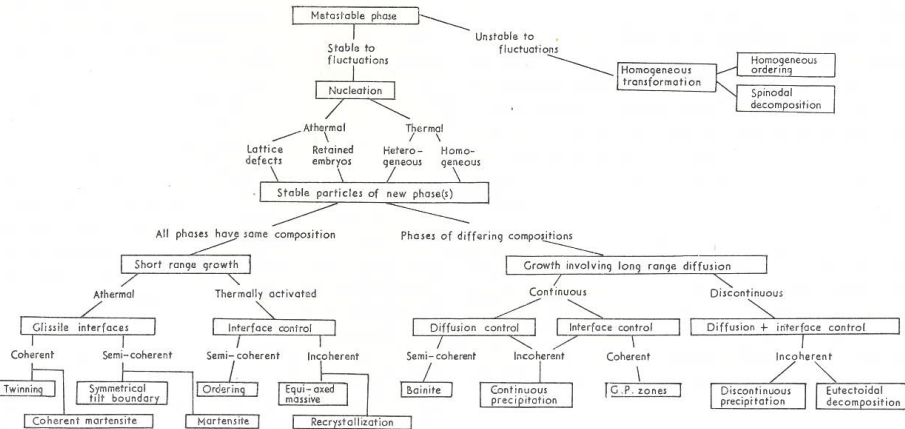
Solvent	Solute	Activation energy, Q (kJ mol ⁻¹)	Frequency factor, D_0 (cm ² s ⁻¹)	Diffusion coefficient, $D_{910^\circ\text{C}}$ (cm ² s ⁻¹)	Temperature range (°C)
γ -iron	C	135	0.15	1.5×10^{-7}	900–1050
	Fe	269	0.18	2.2×10^{-13}	1060–1390
	Co	364	3.0×10^2	24.0×10^{-12} (at 1050°C)	1050–1250
	Cr	405	1.8×10^4	58.0×10^{-12} (at 1050°C)	1050–1250
	Cu	253	3.0	15.0×10^{-11}	800–1200
	Ni	280	0.77	7.7×10^{-13}	930–1050
	P	293	28.3	3.6×10^{-12}	1280–1350
	S	202	1.35	1.5×10^{-9}	1200–1350
	W	376	1.0×10^3	12.0×10^{-12} (at 1050°C)	1050–1250
	α -iron	C	80	6.2×10^{-3}	1.8×10^{-6}
N		76	3.0×10^{-3}	1.3×10^{-6}	
Fe		240	0.5		700–750
Co		226	0.2	2.1×10^{-11}	700–790
Cr		343	3.0×10^4		
Ni		258	9.7	3.7×10^{-11}	700–900
P		230	2.9	2.0×10^{-10}	860–900
W		293	3.8×10^2		

Table 5.2 Diffusion data for microalloy and interstitial solutes in austenite and in ferrite. The diffusion coefficients of these elements at 1200°C in austenite, and at 700°C in ferrite, are also shown

Element/Phase	D_0 ($\text{m}^2 \text{s}^{-1}$)	Q (kJ mol^{-1})	D_α 700°C ($\text{m}^2 \text{s}^{-1}$)	D_γ 1200 °C ($\text{m}^2 \text{s}^{-1}$)
C/ α	0.62×10^{-6}	80.4	3.00×10^{-11}	—
C/ γ	0.10×10^{-4}	135.7	—	1.59×10^{-10}
N/ α	0.50×10^{-6}	77.0	3.66×10^{-11}	—
N/ γ	0.91×10^{-4}	168.6	—	9.60×10^{-11}
Ti/ α	3.15×10^{-4}	248.0	1.56×10^{-17}	—
Ti/ γ	0.15×10^{-4}	251.2	—	1.86×10^{-14}
V/ α	0.61×10^{-4}	267.1	2.80×10^{-19}	—
V/ γ	0.25×10^{-4}	264.2	—	1.07×10^{-14}
Nb/ α	—	—	—	—
Nb/ γ	5.30×10^{-2}	344.6	—	1.56×10^{-13}
Al/ α	0.30×10^{-2}	234.5	7.80×10^{-16}	—
Al/ γ	—	—	—	—
Fe/ α	1.67×10^{-4}	256.7	2.79×10^{-19}	—
Fe/ γ	0.49×10^{-4}	284.1	—	4.13×10^{-15}



Phase transformations in steel



After J. W. Christian

	α'	α_{LB}	α_{UB}	α_a	α_W	α	α_i	P
Nucleation and growth reaction	Y	Y	Y	Y	Y	Y	Y	Y
Plate morphology	Y	Y	Y	Y	Y	N	N	N
IPS shape change with shear component	Y	Y	Y	Y	Y	N	N	N
Diffusionless nucleation	Y	N	N	N	N	N	N	N
Only carbon diffuses during nucleation	N	Y	Y	Y	Y	N	N	N
Reconstructive diffusion during nucleation	N	N	N	N	N	Y	Y	Y
Often nucleates intragranularly on defects	Y	N	N	Y	N	N	Y	Y
Diffusionless growth	Y	Y	Y	Y	N	N	N	N
Reconstructive diffusion during growth	N	N	N	N	N	Y	Y	Y
All atomic correspondence during growth	Y	Y	Y	Y	N	N	N	N
Substitutional atomic correspondence during growth	Y	Y	Y	Y	Y	N	N	N
Bulk redistribution of substitutional atoms during growth	N	N	N	N	N	S	S	S
Local equilibrium at interface during growth	N	N	N	N	N	S	S	S
Local para-equilibrium at interface during growth	N	N	N	N	Y	S	S	N
Diffusion of carbon during transformation	N	N	N	N	Y	Y	Y	Y
Carbon diffusion-controlled growth	N	N	N	N	Y	S	S	S
Cooperative growth of ferrite and cementite	N	N	N	N	N	N	N	Y
High dislocation density	Y	Y	Y	Y	S	N	N	N
Incomplete reaction phenomenon	N	Y	Y	Y	N	N	N	N
Necessarily has a glissile interface	Y	Y	Y	Y	Y	N	N	N
Always has an orientation within the Bain region [†]	Y	Y	Y	Y	Y	N	N	N
Grows across austenite grain boundaries	N	N	N	N	N	Y	Y	Y
High interface mobility at low temperatures	Y	Y	Y	Y	Y	N	N	N
Displacive transformation mechanism	Y	Y	Y	Y	Y	N	N	N
Reconstructive transformation mechanism	N	N	N	N	N	Y	Y	Y

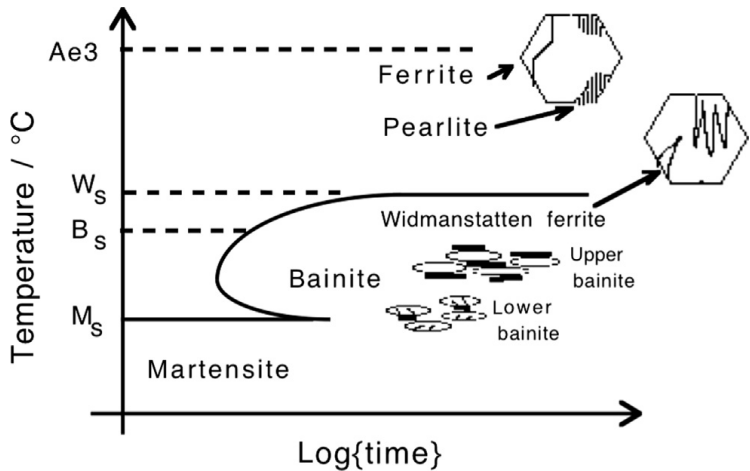
[†] "... a reproducible relation which may be irrational but is close to the rational N-W or K-S relation."

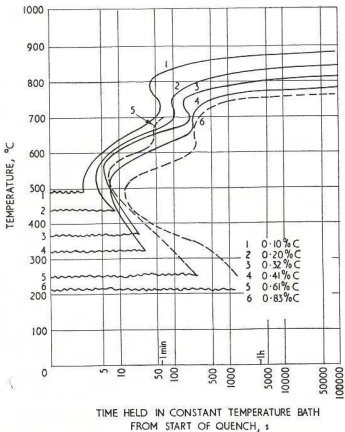
martensite: α' ; lower, upper bainite: α_{LB} , α_{UB} ; acicular, idiomorphic ferrite: α_a , α_i ;

Widmanstätten ferrite: α_W ; allotriomorphic and massive ferrite: α ; pearlite: P

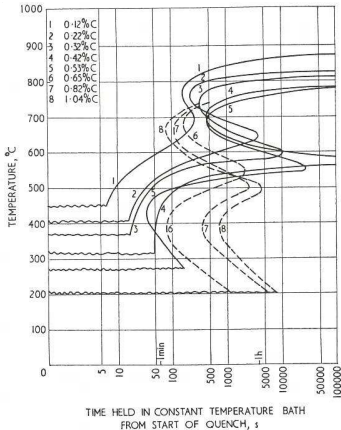
Y: yes; N: no; S: sometimes

TTT diagrams

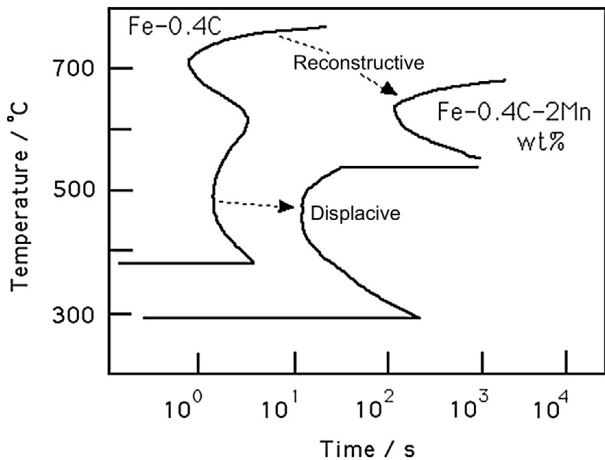




Effect of carbon content on the isothermal transformation diagrams of $\frac{1}{2}\%$ Mo-B steels; 0% curves only are shown



13 Effect of carbon content on the isothermal transformation diagrams of 1% Cr- $\frac{1}{2}\%$ Mo-B steels; 0% curves only are shown



Decomposition of austenite

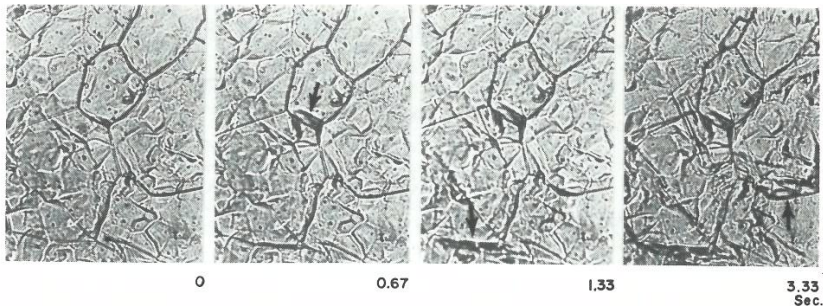


Fig. 5. Cinephotomicrographic sequence showing the formation of ferrite allotromorphs (arrows) on austenite grain boundaries in pure iron at 825°C (cooling rate 12°C/s) (x 125).⁽⁸⁾

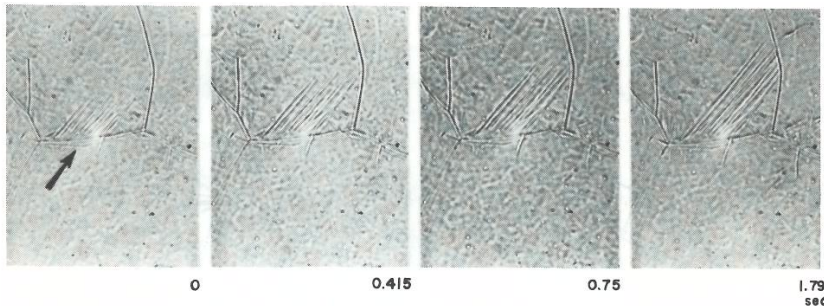


Fig. 6. Cinematographic sequence showing the growth of Widmanstätten ferrite (arrow) from Fe-0.8C austenite at 617°C (cooling rate of 10°C/s) (x 250).⁽⁸⁾

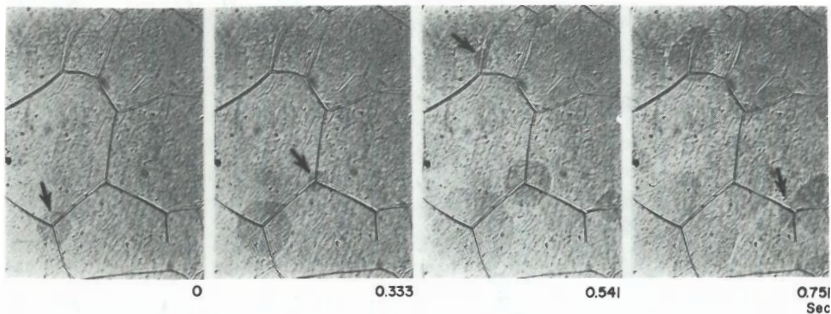


Fig. 8. Cinephotomicrographic sequence of growth of a pearlite nodule (arrow) at the junction of three austenite grains; cooling rate 4800°F and transformation temperature 1090°F . Magnification about 250 times. (9)

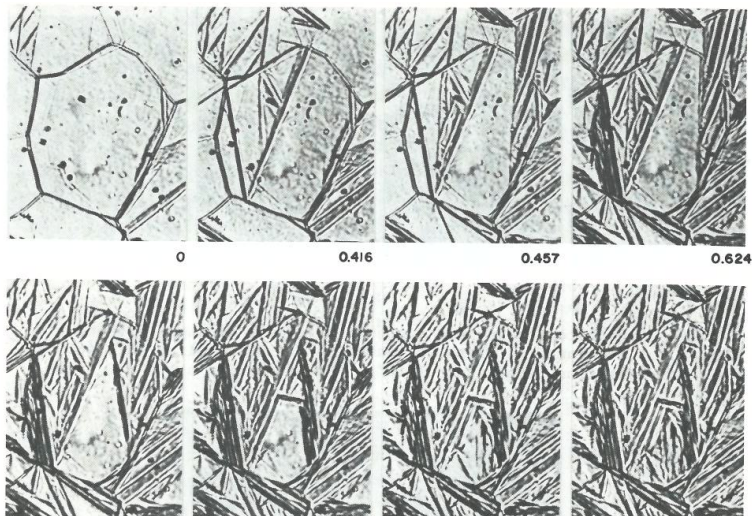


Fig. 10. Cinephotomicrographic sequence showing the formation of lath martensite in a low-alloy steel at 330°C (cooling rate of 17°C/s) (x227).(8)

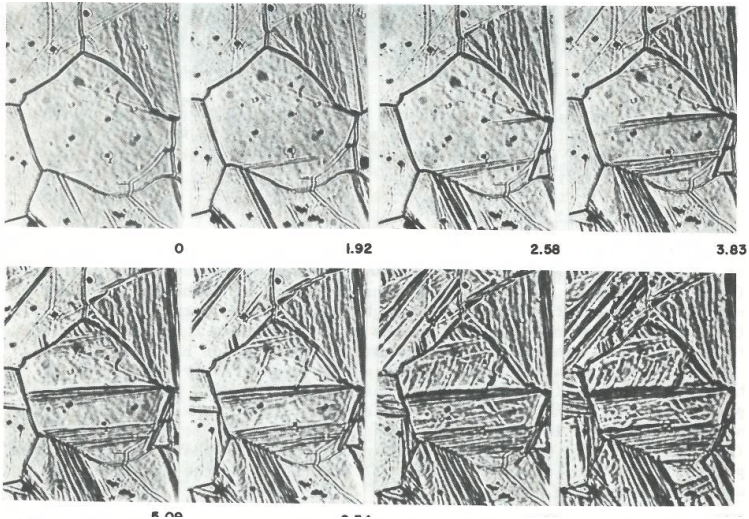
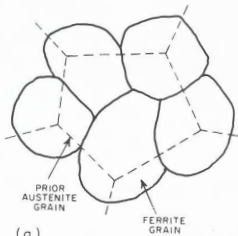
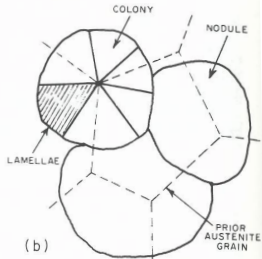


Fig. 11. Cinephotomicrographic sequence showing the formation of bainite in a low-alloy steel at 550°C (cooling rate 6.2°C/s)(x227). (8)

FERRITE



PEARLITE



BAINITE or LATH MARTENSITE

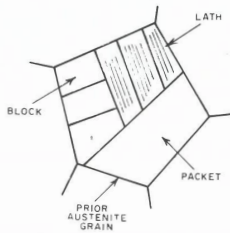
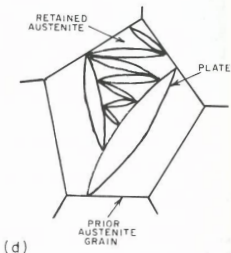
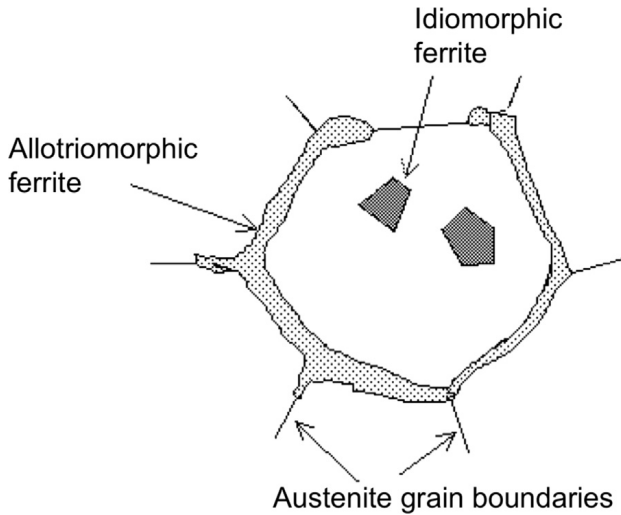
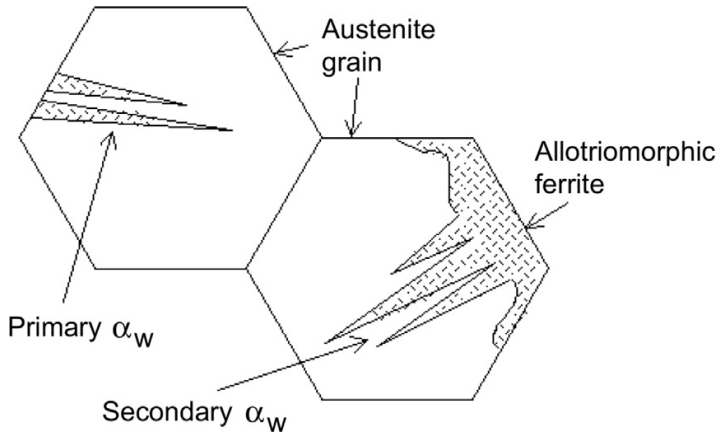


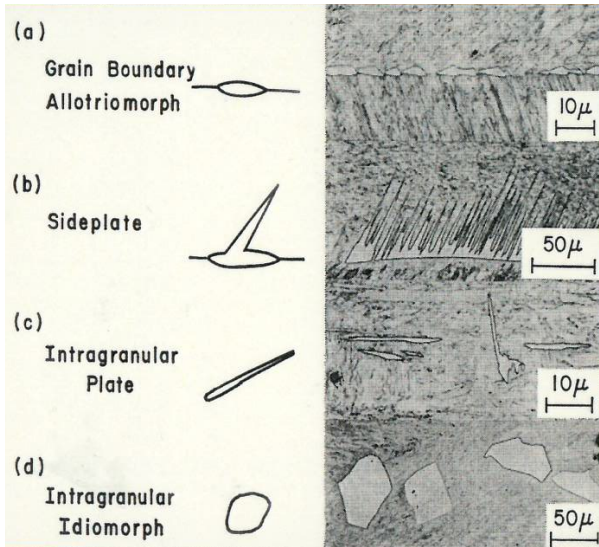
PLATE MARTENSITE



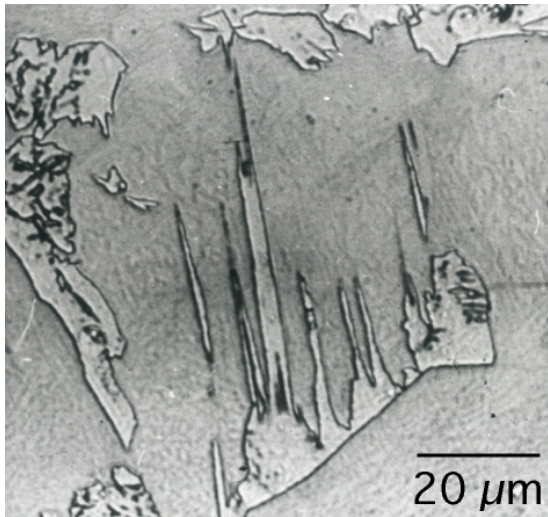
Growth of proeutectoid ferrite

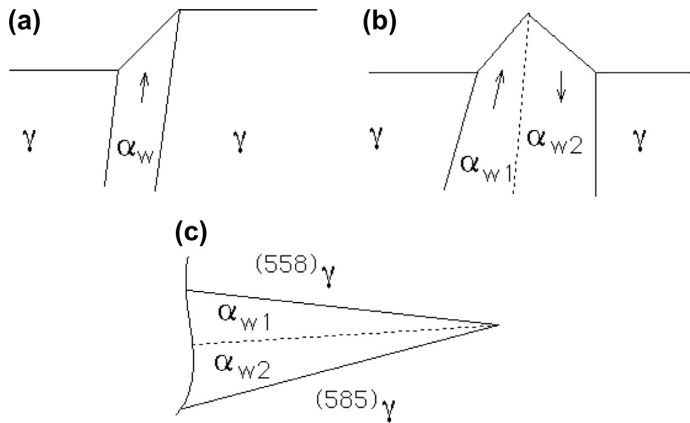


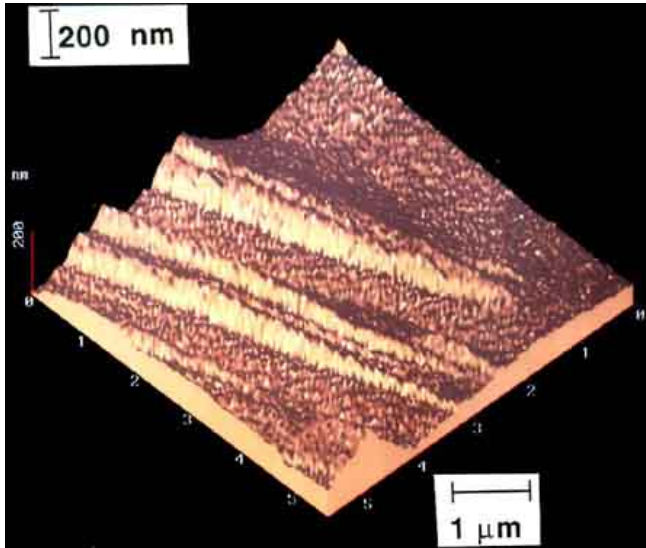




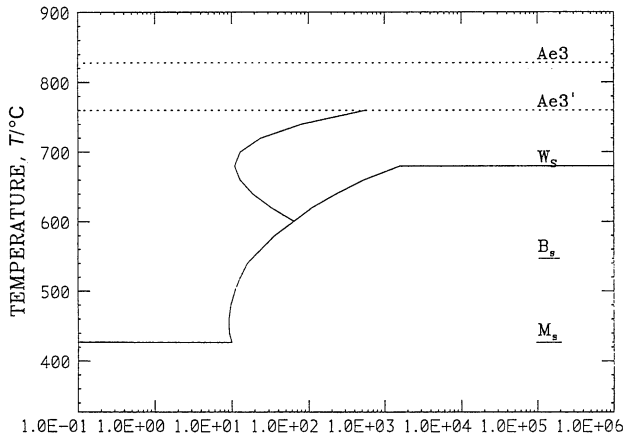
Widmanstätten ferrite



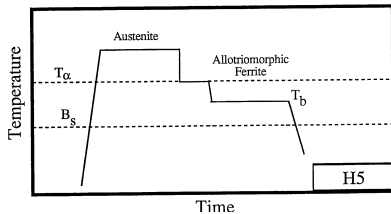
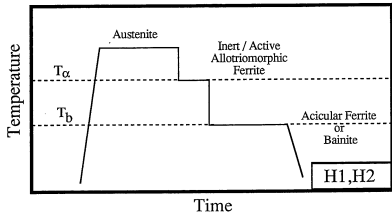
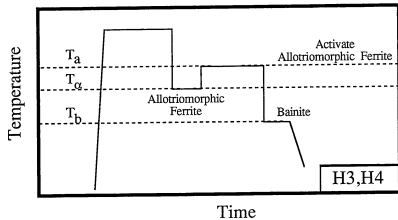
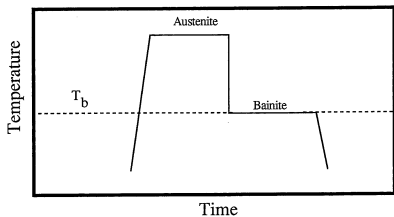




Acicular ferrite



Calculated TTT for TIME, t/s
0.1C-0.68Si-1.24Mn-0.04Ni-0.01Mo-1.87Cr-0.007Al-0.015Ti
(274ppm O 168ppm N)



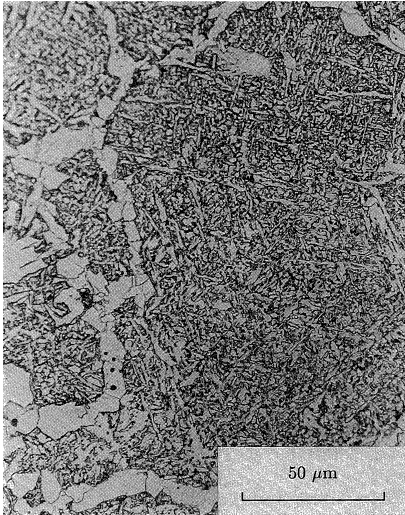


Fig. 7 The microstructure generated by heat-treatment H1. The allotropic ferrite layer is inert, giving acicular ferrite in the interiors of the austenite grains.

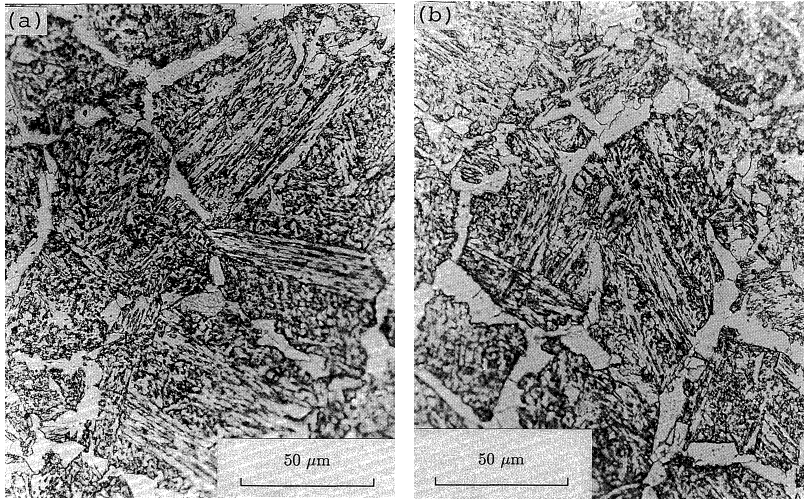


Fig. 9 The microstructures generated by heat-treatments H3 (a) and H4 (b), where the allotriomorphic ferrite was activated by annealing at 760 and 750°C, respectively. Bainite sheaves have formed as a consequence.

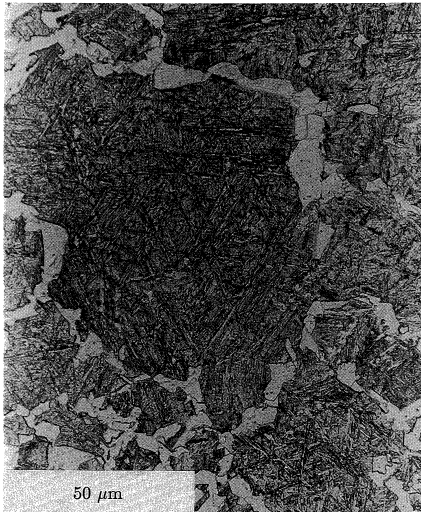


Fig. 10 The microstructure generated by heat-treatment H5, consisting of allotriomorphic ferrite and martensite, since isothermal holding at a temperature above B_s did not cause any transformation.

Decomposition of austenite

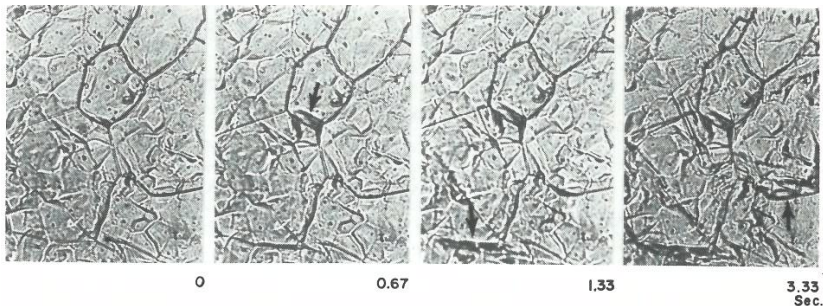


Fig. 5. Cinphotomicrographic sequence showing the formation of ferrite allotromorphs (arrows) on austenite grain boundaries in pure iron at 825°C (cooling rate 12°C/s) (x 125).⁽⁸⁾

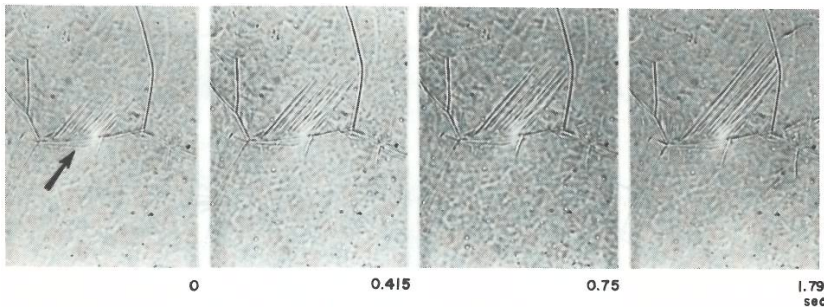


Fig. 6. Cinephotomicrographic sequence showing the growth of Widmanstätten ferrite (arrow) from Fe-0.8C austenite at 617°C (cooling rate of 10°C/s) (x 250).⁽⁸⁾

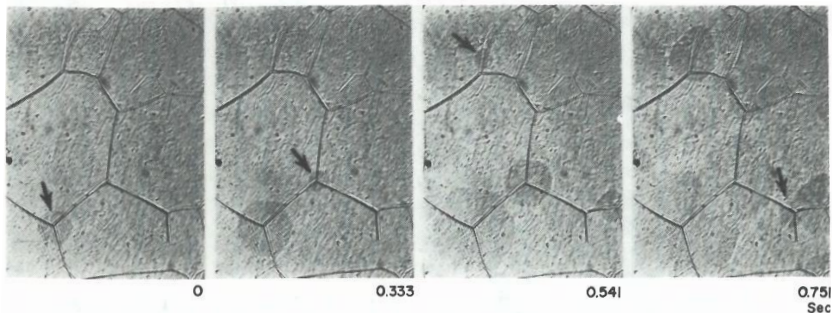


Fig. 8. Cinephotomicrographic sequence of growth of a pearlite nodule (arrow) at the junction of three austenite grains; cooling rate 4800°F and transformation temperature 1090°F . Magnification about 250 times. ⁽⁹⁾

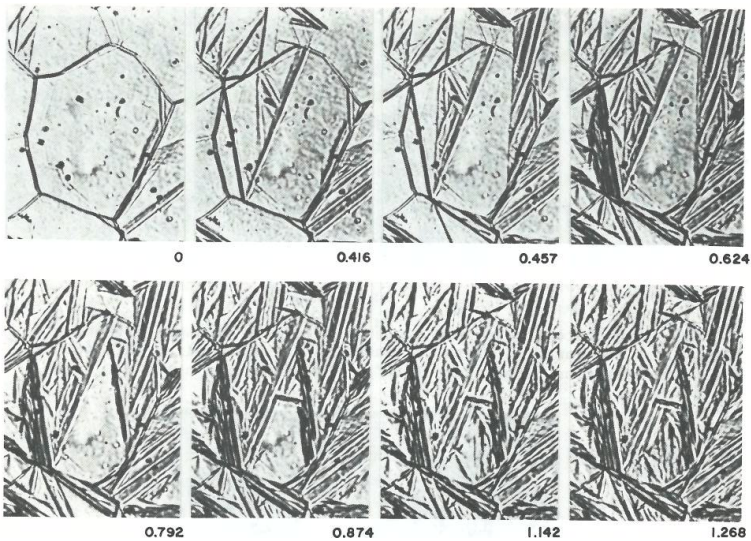


Fig. 10. Cinephotomicrographic sequence showing the formation of 1
martensite in a low-alloy steel at 330°C (cooling rate of 17°C/s)
(x227).(8)

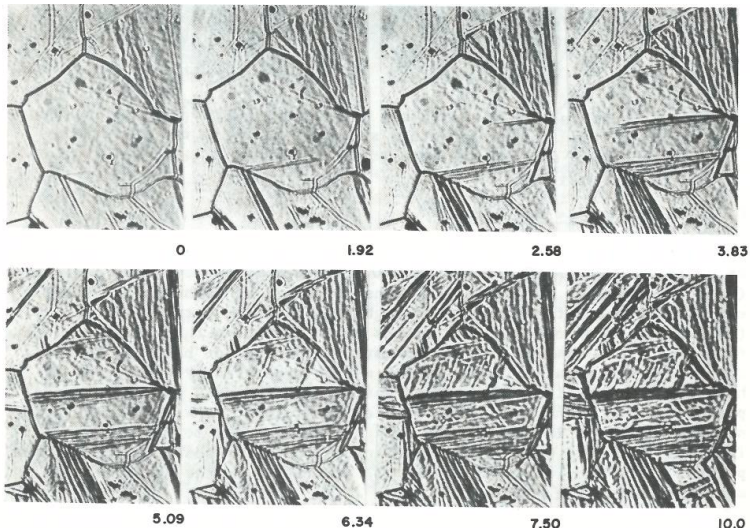
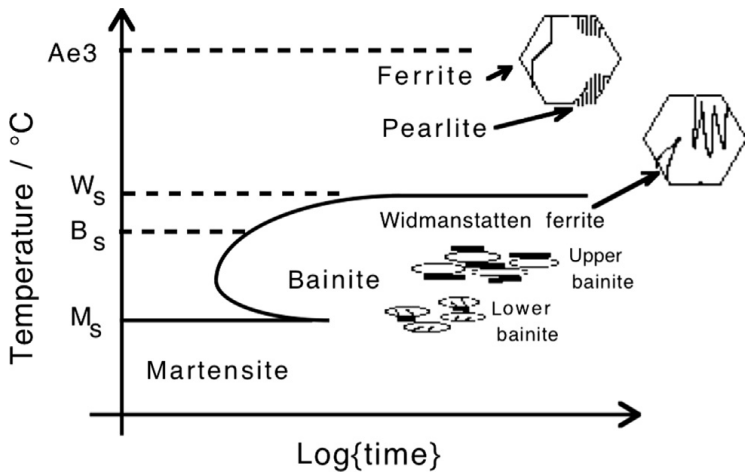
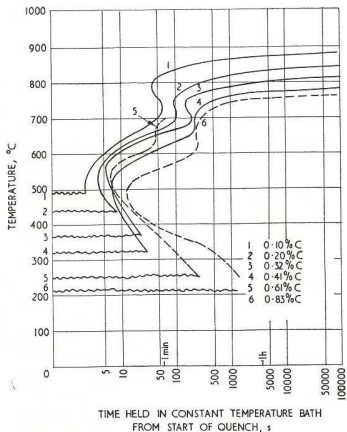


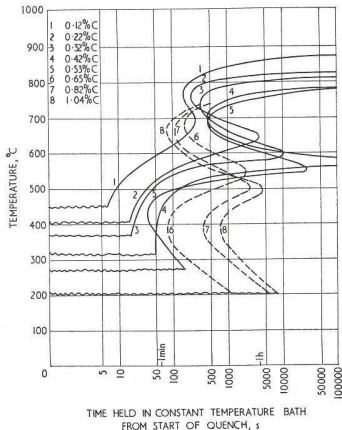
Fig. 11. Cinephotomicrographic sequence showing the formation of bainite in a low-alloy steel at 550°C (cooling rate 6.2°C/s)(x227).

TTT diagrams

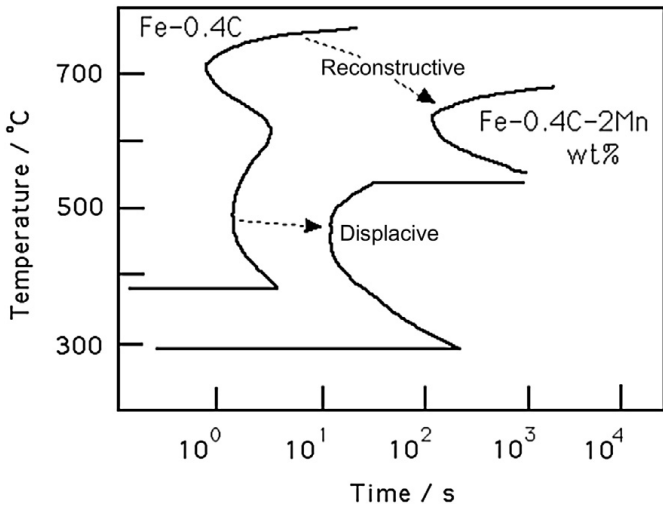




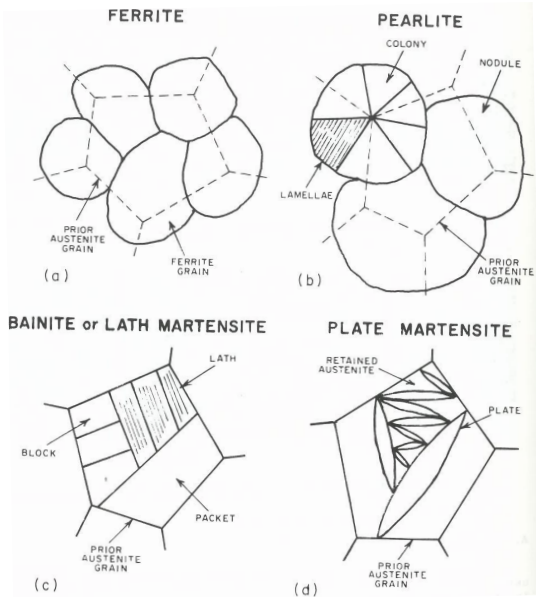
Effect of carbon content on the isothermal transformation diagrams of $\frac{1}{2}\%$ Mo-B steels; 0% curves only are shown



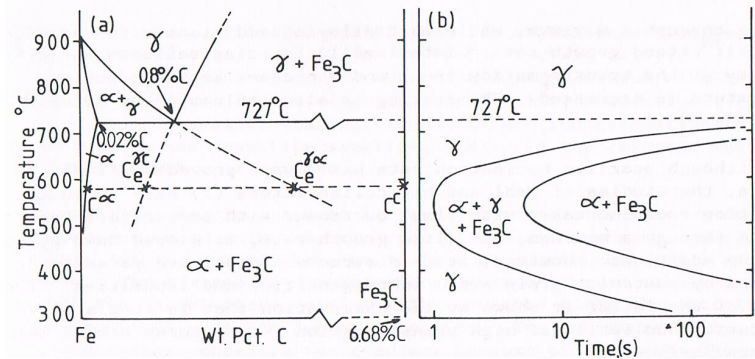
13 Effect of carbon content on the isothermal transformation diagrams of 1% Cr- $\frac{1}{2}\%$ Mo-B steels; 0% curves only are shown

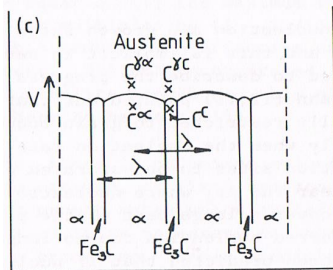
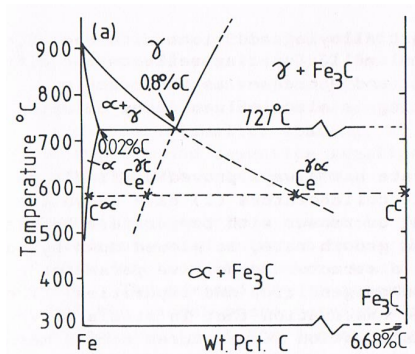


Decomposition of austenite by reconstructive transformation



Growth of pearlite

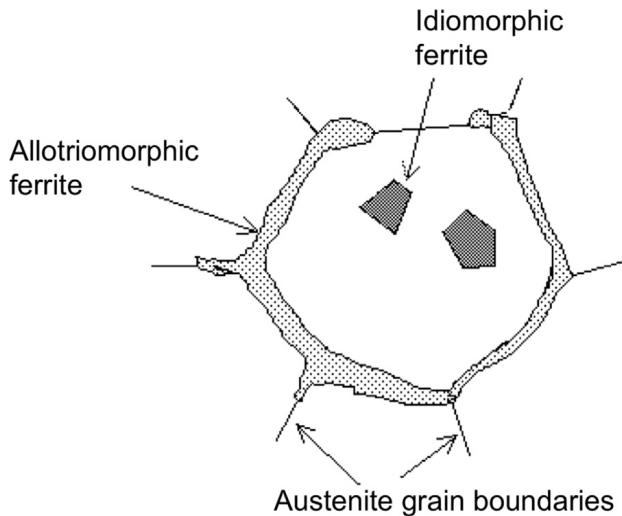


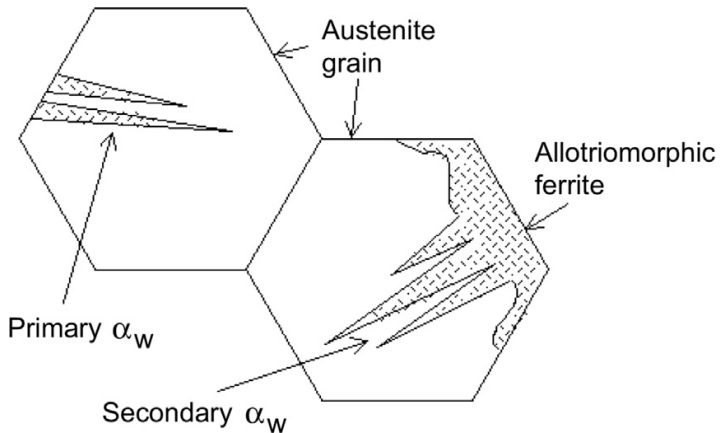


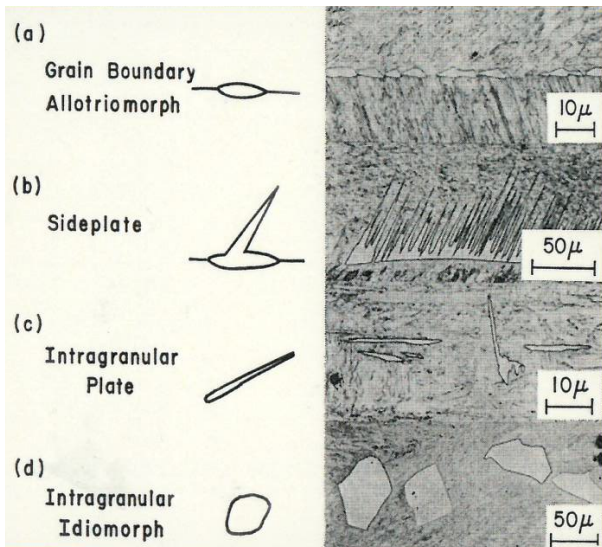
$$V \approx D \frac{\lambda}{2\lambda^{\alpha}\lambda^{\text{C}}} \frac{C_e^{\gamma\alpha} - C_e^{\gamma\text{C}}}{C^{\text{C}} - C^{\alpha}} \quad [\text{m s}^{-1}]$$

D is carbon diffusivity in austenite; λ^{α} , λ^{C} are widths of ferrite and cementite lamella.

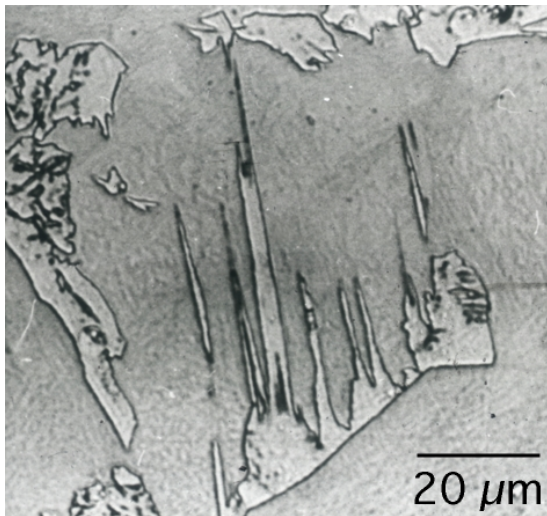
Growth of proeutectoid ferrite

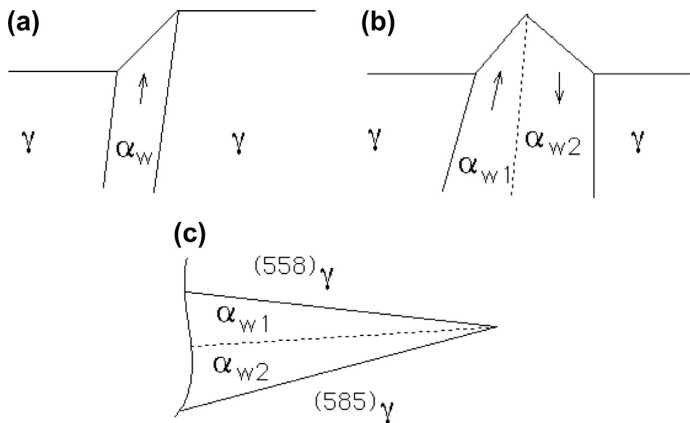


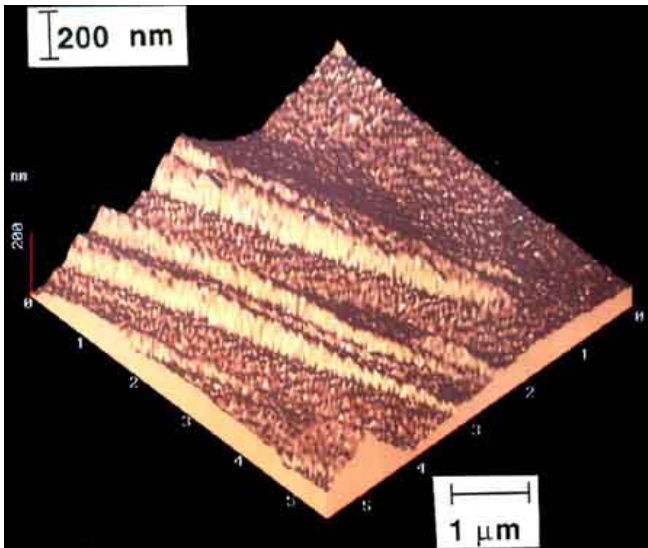




Widmanstätten ferrite







	α'	α_{LB}	α_{UB}	α_a	α_W	α	α_i	P
Nucleation and growth reaction	Y	Y	Y	Y	Y	Y	Y	Y
Plate morphology	Y	Y	Y	Y	Y	N	N	N
IPS shape change with shear component	Y	Y	Y	Y	Y	N	N	N
Diffusionless nucleation	Y	N	N	N	N	N	N	N
Only carbon diffuses during nucleation	N	Y	Y	Y	Y	N	N	N
Reconstructive diffusion during nucleation	N	N	N	N	N	Y	Y	Y
Often nucleates intragranularly on defects	Y	N	N	Y	N	N	Y	Y
Diffusionless growth	Y	Y	Y	Y	N	N	N	N
Reconstructive diffusion during growth	N	N	N	N	N	Y	Y	Y
All atomic correspondence during growth	Y	Y	Y	Y	N	N	N	N
Substitutional atomic correspondence during growth	Y	Y	Y	Y	Y	N	N	N
Bulk redistribution of substitutional atoms during growth	N	N	N	N	N	S	S	S
Local equilibrium at interface during growth	N	N	N	N	N	S	S	S
Local para-equilibrium at interface during growth	N	N	N	N	Y	S	S	N
Diffusion of carbon during transformation	N	N	N	N	Y	Y	Y	Y
Carbon diffusion-controlled growth	N	N	N	N	Y	S	S	S
Cooperative growth of ferrite and cementite	N	N	N	N	N	N	N	Y
High dislocation density	Y	Y	Y	Y	S	N	N	N
Incomplete reaction phenomenon	N	Y	Y	Y	N	N	N	N
Necessarily has a glissile interface	Y	Y	Y	Y	Y	N	N	N
Always has an orientation within the Bain region [†]	Y	Y	Y	Y	Y	N	N	N
Grows across austenite grain boundaries	N	N	N	N	N	Y	Y	Y
High interface mobility at low temperatures	Y	Y	Y	Y	Y	N	N	N
Displacive transformation mechanism	Y	Y	Y	Y	Y	N	N	N
Reconstructive transformation mechanism	N	N	N	N	N	Y	Y	Y

[†] "... a reproducible relation which may be irrational but is close to the rational N-W or K-S relation."

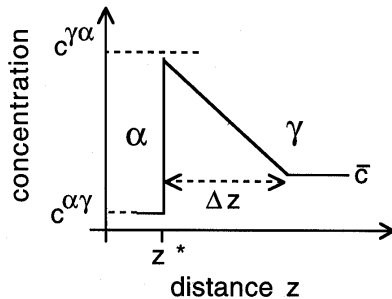
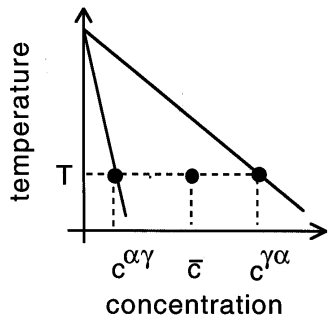
martensite: α' ; lower, upper bainite: α_{LB} , α_{UB} ; acicular, idiomorphic ferrite: α_a , α_i ;

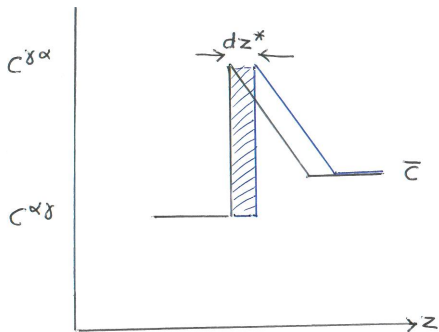
Widmanstätten ferrite: α_W ; allotriomorphic and massive ferrite: α ; pearlite: P

Y: yes; N: no; S: sometimes

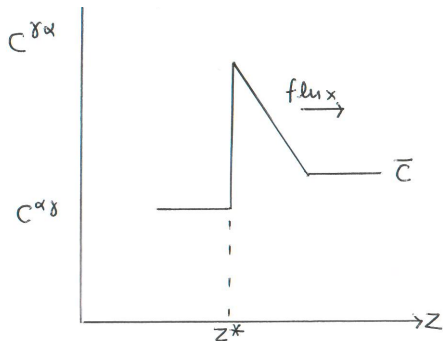
After H. K. D. H. Bhadeshia and J. W. Christian

The rate of growth of ferrite in austenite



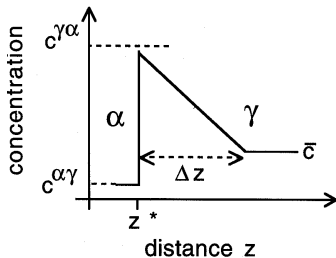


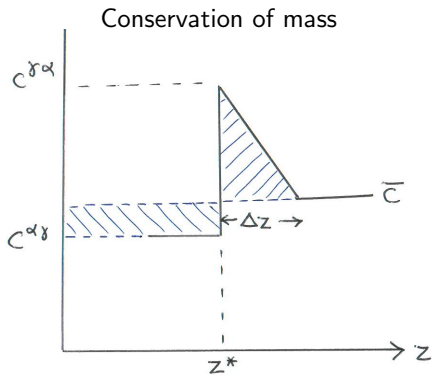
$$\text{Rate of solute partitioning} = (c^{\gamma\alpha} - c^{\alpha\gamma}) \frac{\partial z^*}{\partial t}$$



Diffusive flux
away from interface $= -D \frac{\partial c}{\partial z}$

$$\begin{aligned}
 \text{Rate of solute partitioning} &= \text{Diffusive flux away from interface} \\
 (c^{\gamma\alpha} - c^{\alpha\gamma}) \frac{\partial z^*}{\partial t} &= -D \frac{\partial c}{\partial z} \\
 &\approx -D \frac{\bar{c} - c^{\gamma\alpha}}{\Delta z}
 \end{aligned}$$





$$(\bar{c} - c^{\alpha\gamma}) z^* = \frac{1}{2} (c^{\gamma\alpha} - \bar{c}) \Delta z$$

Combining diffusion controlled interface velocity equation

$$(c^{\gamma\alpha} - c^{\alpha\gamma}) \frac{\partial z^*}{\partial t} \approx -D \frac{\bar{c} - c^{\gamma\alpha}}{\Delta z}$$

with conservation of mass condition

$$(\bar{c} - c^{\alpha\gamma}) z^* = \frac{1}{2} (c^{\gamma\alpha} - \bar{c}) \Delta z$$

leads to

$$\frac{\partial z^*}{\partial t} = \frac{D (c^{\gamma\alpha} - \bar{c})^2}{2z^* (c^{\gamma\alpha} - c^{\alpha\gamma}) (\bar{c} - c^{\alpha\gamma})}$$

that is, $z^* \propto \sqrt{Dt}$

In the single component case,

$$\begin{array}{l} \text{Rate of solute} \\ \text{partitioning} \end{array} = \begin{array}{l} \text{Diffusive flux} \\ \text{away from interface} \end{array}$$
$$(c^{\gamma\alpha} - c^{\alpha\gamma}) \frac{\partial z^*}{\partial t} = (c^{\gamma\alpha} - c^{\alpha\gamma}) v = -D \frac{\partial c}{\partial z}$$

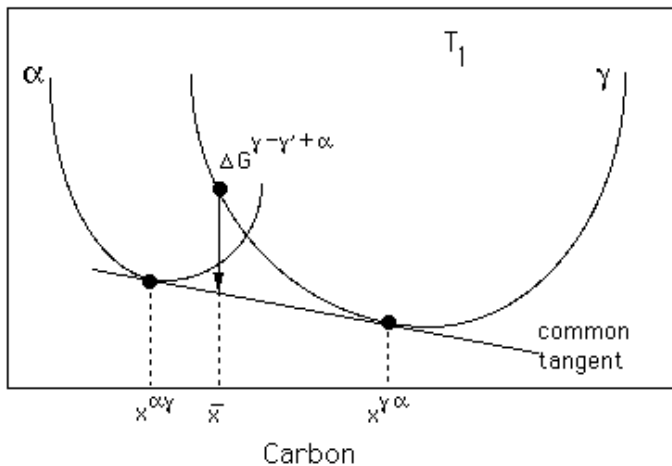
In the case of two components, say C and Mn,

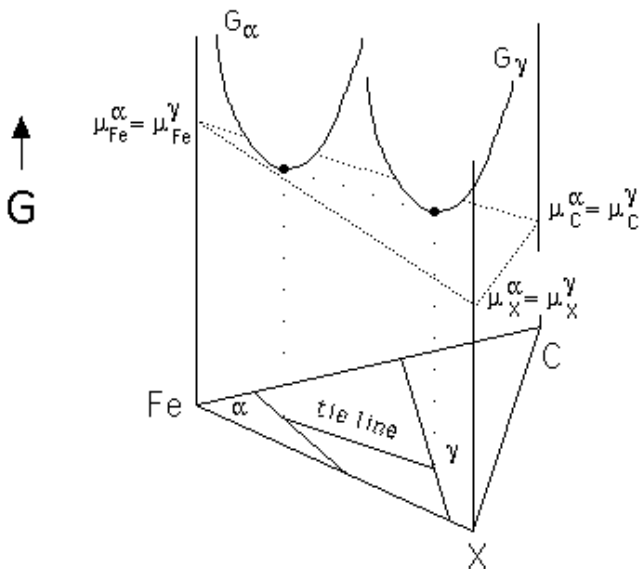
$$(c_C^{\gamma\alpha} - c_C^{\alpha\gamma}) v = -D_C^\gamma \frac{\partial c_C}{\partial z}$$
$$(c_{\text{Mn}}^{\gamma\alpha} - c_{\text{Mn}}^{\alpha\gamma}) v = -D_{\text{Mn}}^\gamma \frac{\partial c_{\text{Mn}}}{\partial z}$$

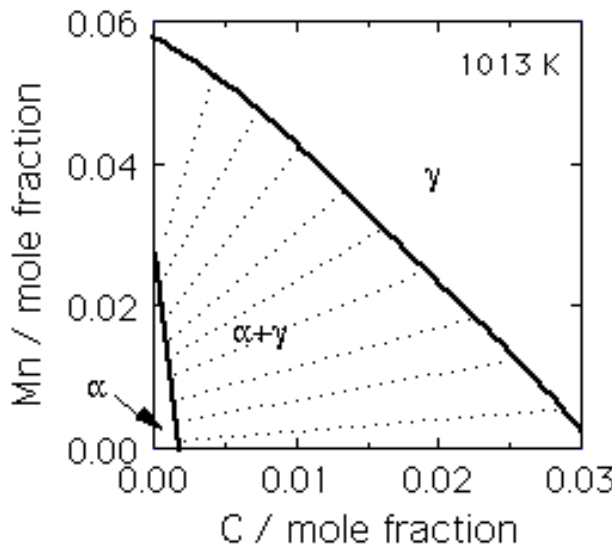
But

$$D_C^\gamma \gg D_{\text{Mn}}^\gamma$$

Gibbs free energy per mole

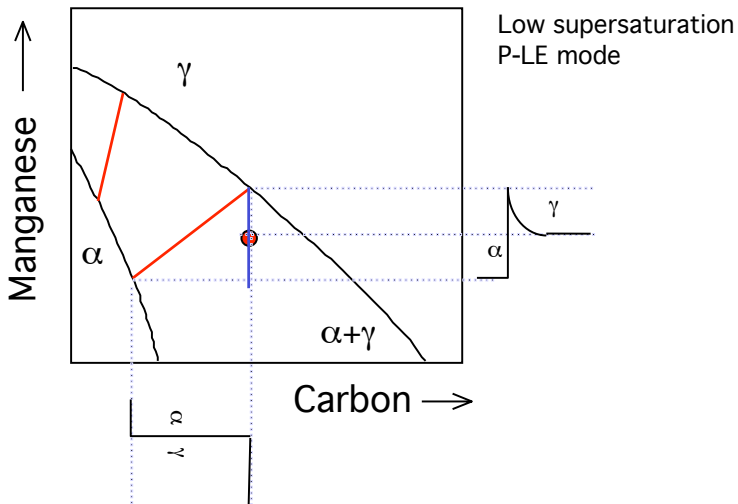


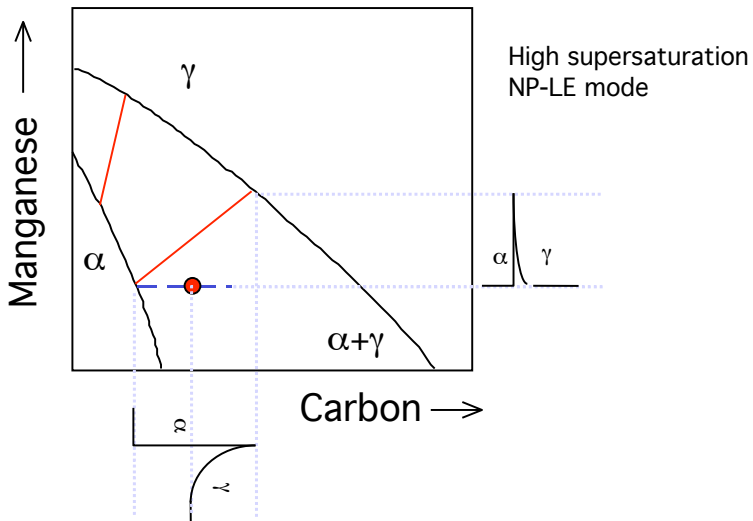




$$(c_C^{\gamma\alpha} - c_C^{\alpha\gamma}) v = -D_C^\gamma \frac{\partial c_C}{\partial z}$$

$$(c_{Mn}^{\gamma\alpha} - c_{Mn}^{\alpha\gamma}) v = -D_{Mn}^\gamma \frac{\partial c_{Mn}}{\partial z}$$



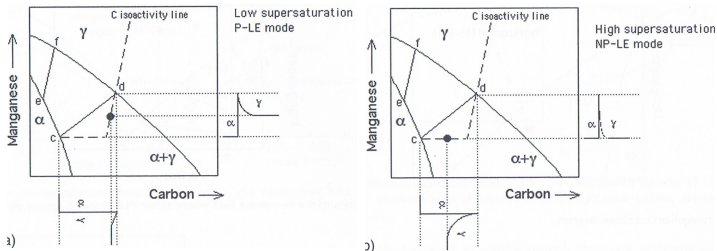


There is *local equilibrium* at the α/γ interface: compositions in both α and γ are those at the ends of equilibrium tie lines.

Austenite and ferrite cannot *both* have concentrations of C or Mn *greater* than the average \bar{c} . Therefore there is a unique solution to the coupled equations on slide 8.

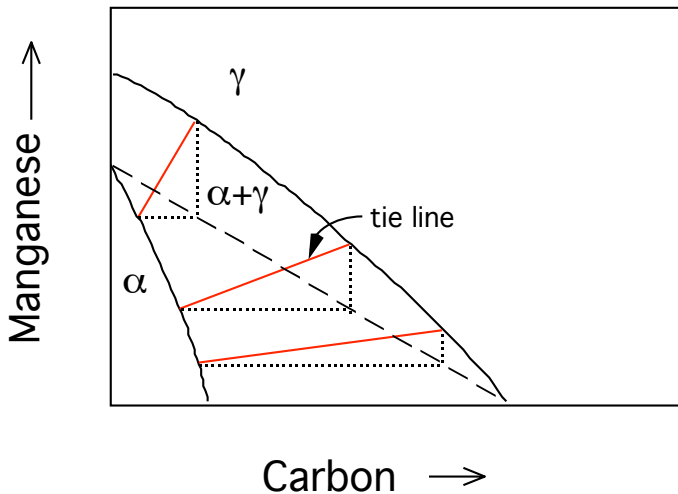
At low undercooling and supersaturation growth is by
Partitioning-Local Equilibrium mode

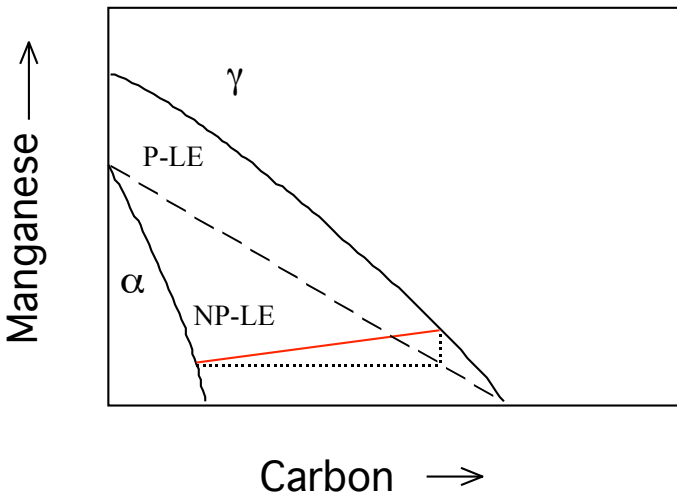
At high undercooling and supersaturation growth is by
Negligible Partitioning-Local Equilibrium mode

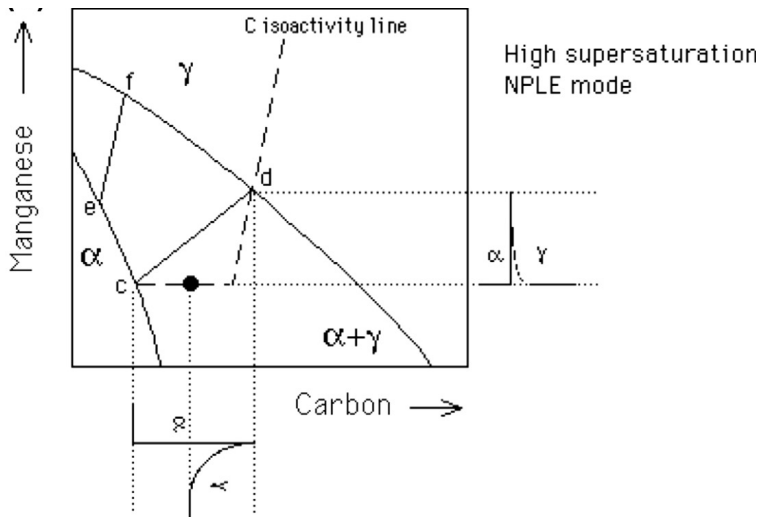


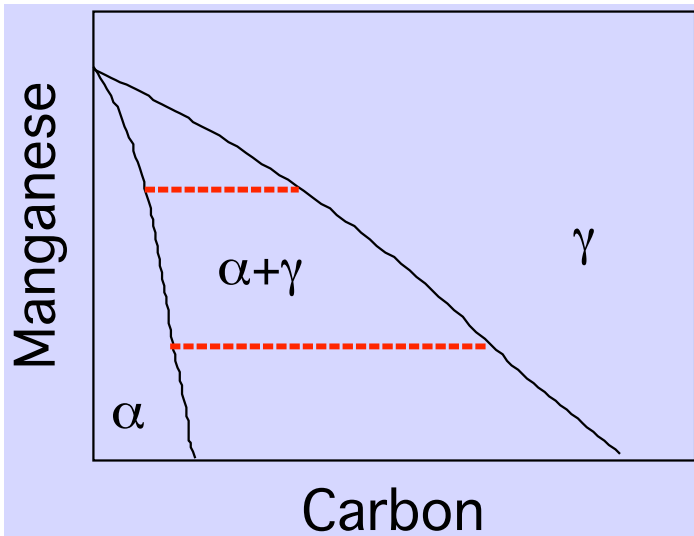
$$(c_C^{\gamma\alpha} - c_C^{\alpha\gamma}) v = -D_C^\gamma \frac{\partial c_C}{\partial z}$$

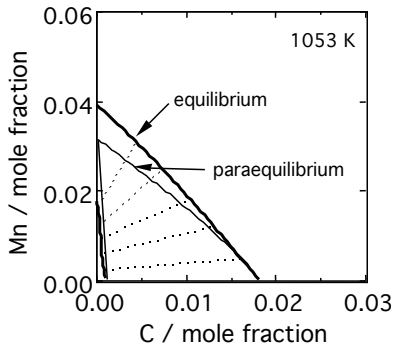
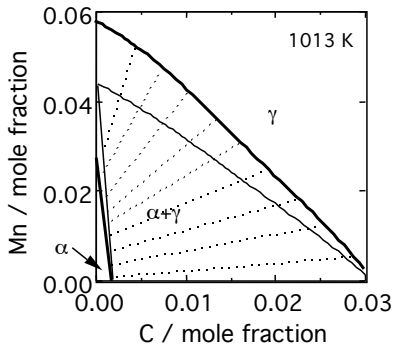
$$(c_{Mn}^{\gamma\alpha} - c_{Mn}^{\alpha\gamma}) v = -D_{Mn}^\gamma \frac{\partial c_{Mn}}{\partial z}$$

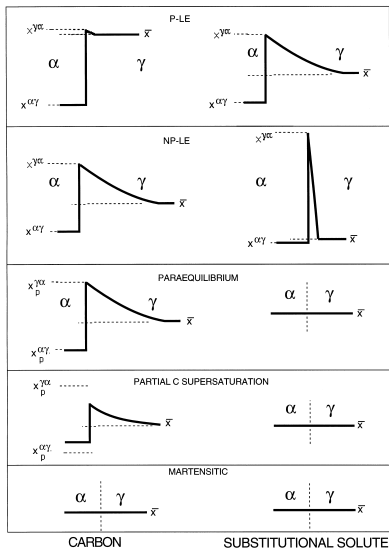




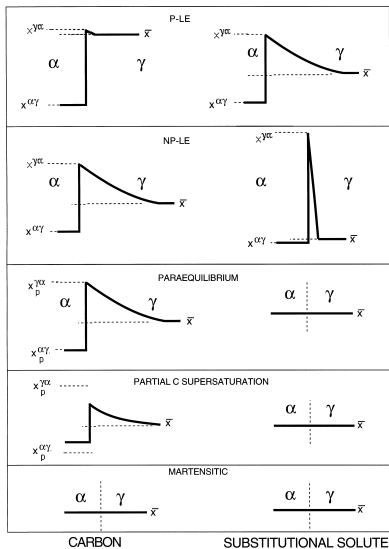




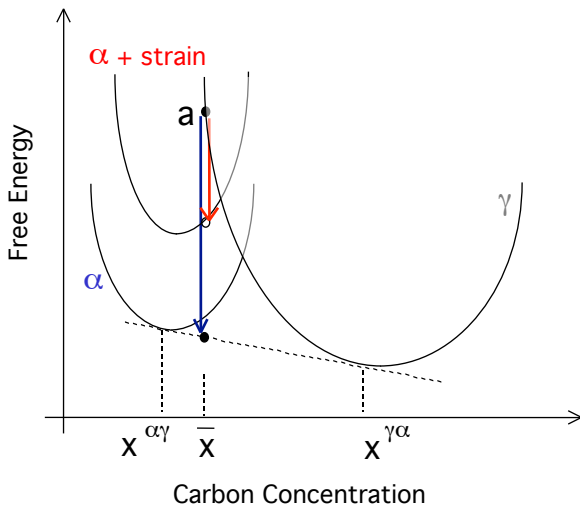


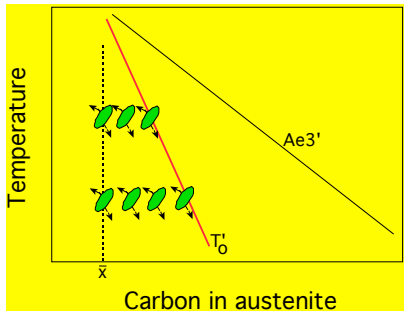
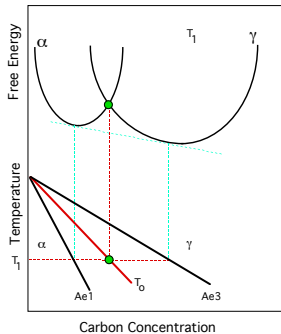


Decomposition of austenite by displacive transformation



Bainite





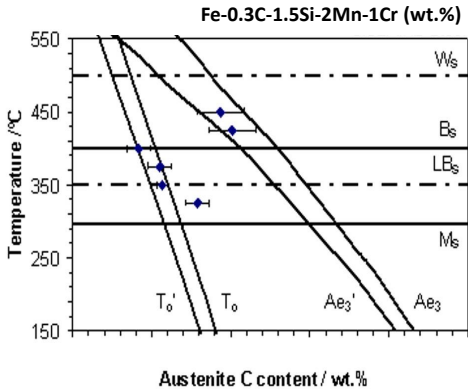
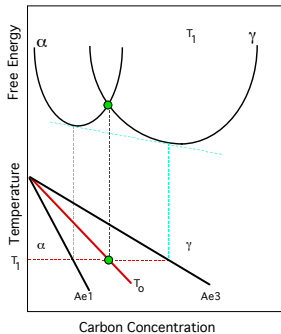
Above T_0 : Widmanstätten ferrite

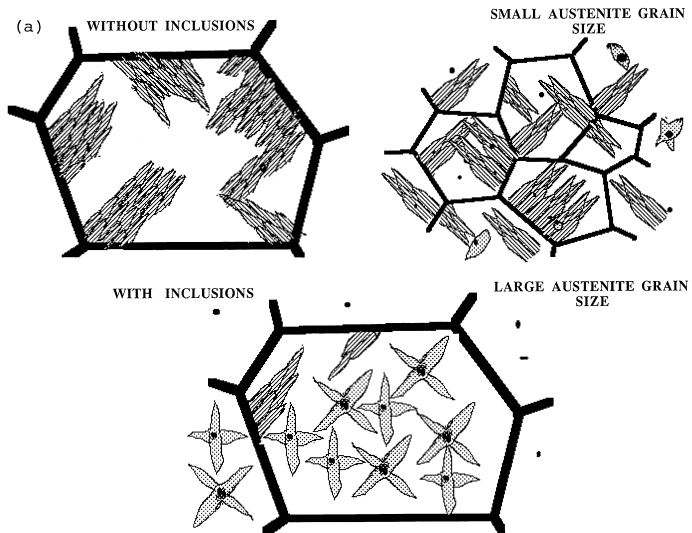
Below T_0 : bainite

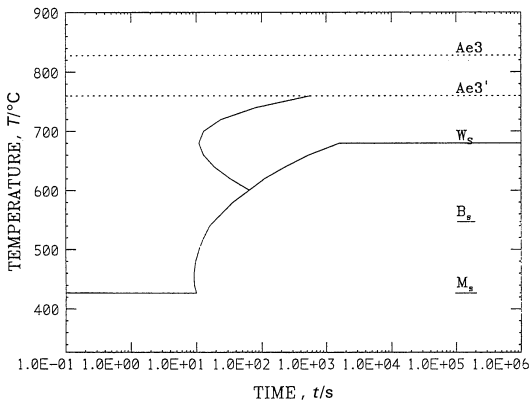
Upper bainite — carbon rejected into austenite

Lower bainite — carbide retained in bainite ($\approx 60^\circ$ to midrib)

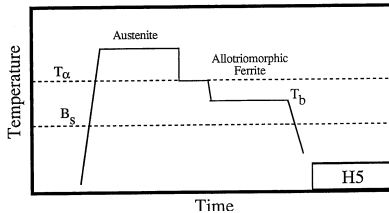
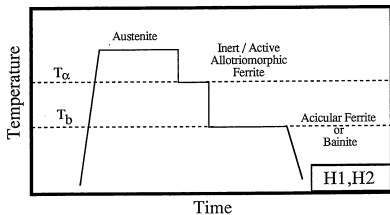
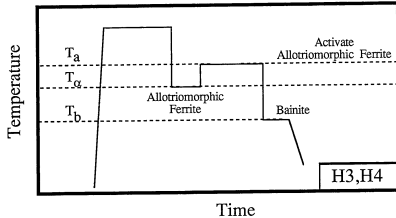
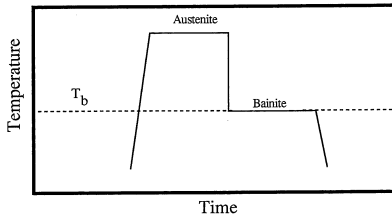
Acicular ferrite — bainite nucleated inside austenite grains







Calculated TTT for
0.1C-0.68Si-1.24Mn-0.04Ni-0.01Mo-1.87Cr-0.007Al-0.015Ti
(274ppm O 168ppm N)



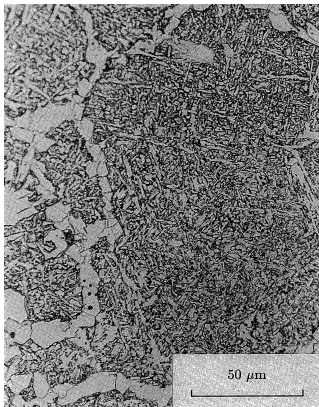


Fig. 7 The microstructure generated by heat-treatment H1. The allotropic ferrite layer is inert, giving acicular ferrite in the interiors of the austenite grains.

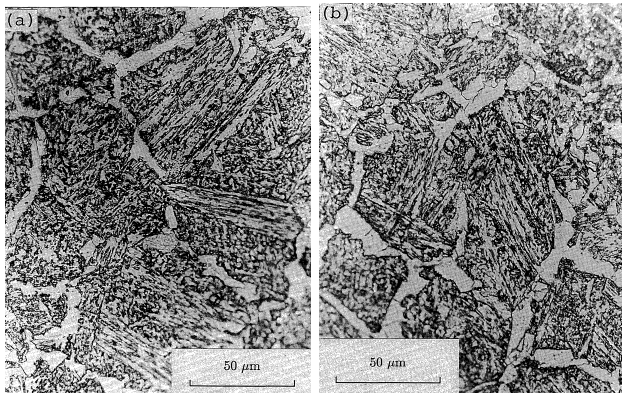


Fig. 9 The microstructures generated by heat-treatments H3 (a) and H4 (b), where the allotriomorphic ferrite was activated by annealing at 760 and 750°C, respectively. Bainite sheaves have formed as a consequence.

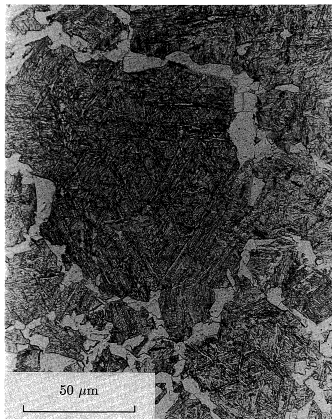


Fig. 10 The microstructure generated by heat-treatment H5, consisting of allotriomorphic ferrite and martensite, since isothermal holding at a temperature above B_S did not cause any transformation.

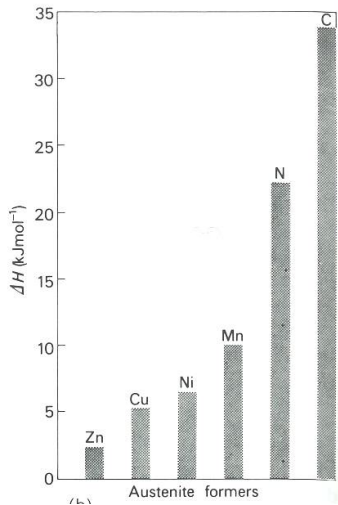
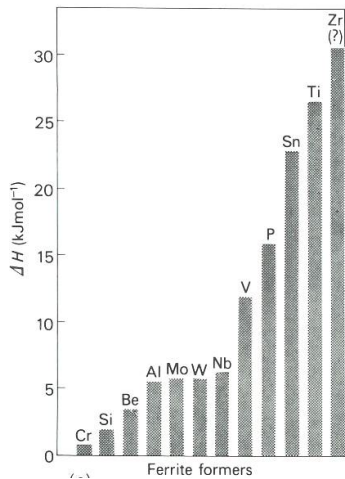
Homework for next week

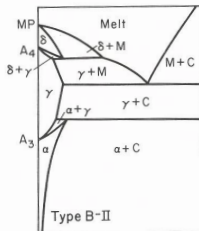
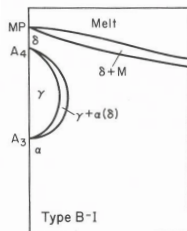
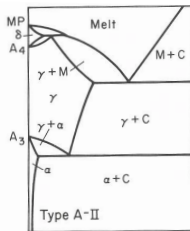
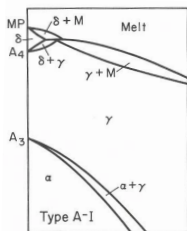
watch these videos

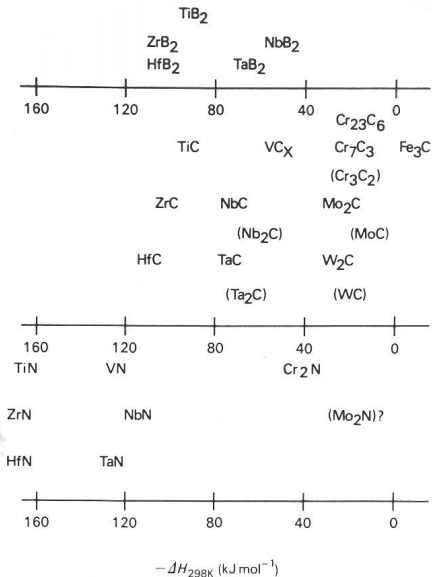
<https://www.youtube.com/watch?v=FffY381eMhU>

<https://www.youtube.com/watch?v=S-5ZMhE7lak>

Alloy steels







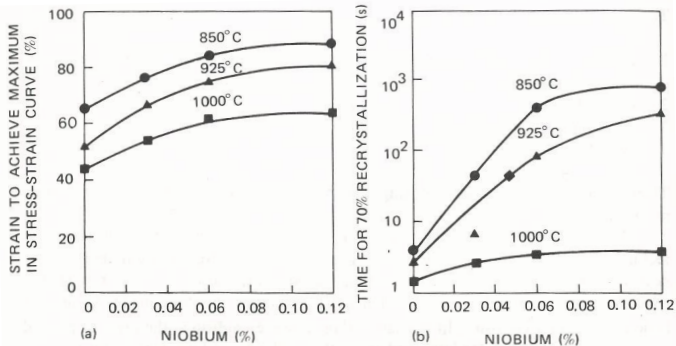
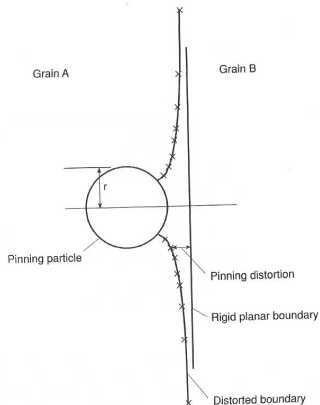


Figure VI-1. Effect of niobium on the recrystallization of a 0.05%C-1.8%Mn steel. (a) Dynamic recrystallization. (b) Static recrystallization. (L. Meyer, F. Heisterkamp, and W. Mueschenborn, in *Microalloying 75*, Union Carbide Corp., New York, 1976, p. 153, by permission.)



$$\text{Zener's pinning force : } p = \pi r \gamma$$

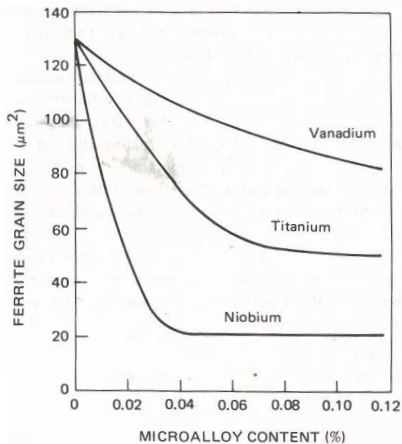
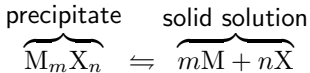


Figure VI-2. Effect of microalloy content (niobium, vanadium, or titanium) on the ferrite grain size of as-hot-rolled low-carbon steel strip. (L. Meyer, F. Heisterkamp, and W. Mueschenborn, in *Microalloying 75*, Union Carbide Corp., New York, 1976, p. 153, by permission.)

Order of solubility of carbide in austenite: $\text{V} \rightarrow \text{Ti} \rightarrow \text{Nb}$

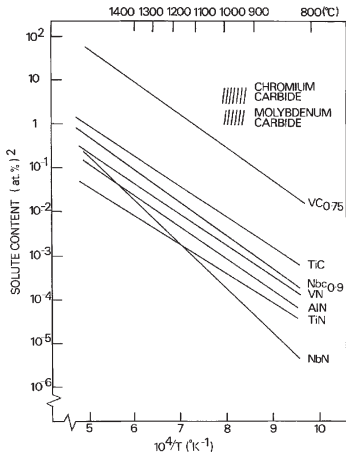


$$\begin{aligned} \text{equilibrium constant} : K &= \frac{a_M^m a_X^n}{a_{M_m X_n}} \propto \overbrace{[\text{wt}\%M]^m [\text{wt}\%X]^n}^{\text{dissolved}} \\ &\equiv k_s : \begin{array}{l} \text{solubility} \\ \text{product} \end{array} \end{aligned}$$

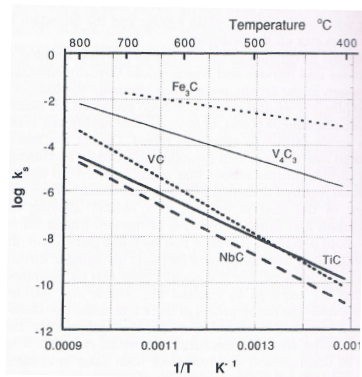
$$RT \ln K = m\bar{\mu}_M + n\bar{\mu}_X - \bar{\mu}_{M_m X_n}$$

$$\ln k_s = -(Q/RT) + \text{constant}$$

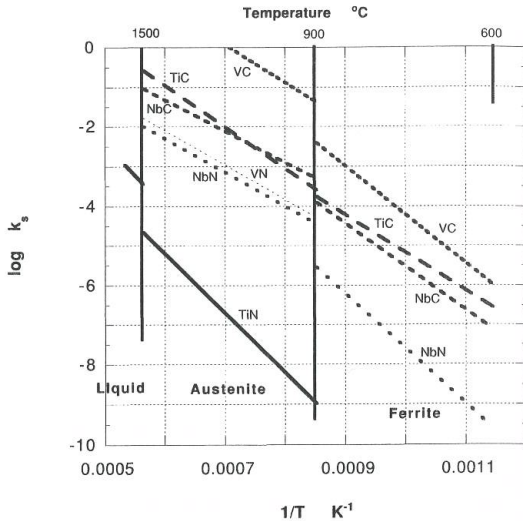
$$\log k_s = A - B/T$$

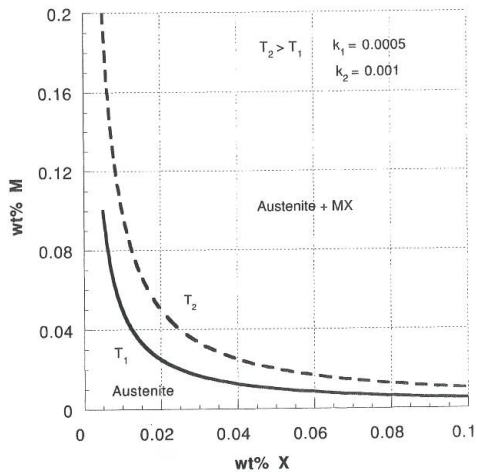


Austenite



Ferrite





V_T : wt% V in alloy

N_T : wt% N in alloy

$[V]$: wt% V dissolved in austenite

$[N]$: wt% N dissolved in austenite

V_{VN} : wt% V present as VN

N_{VN} : wt% N present as VN

A_V : relative atomic mass of V

A_N : relative atomic mass of N

$$V_T = [V] + V_{VN}$$

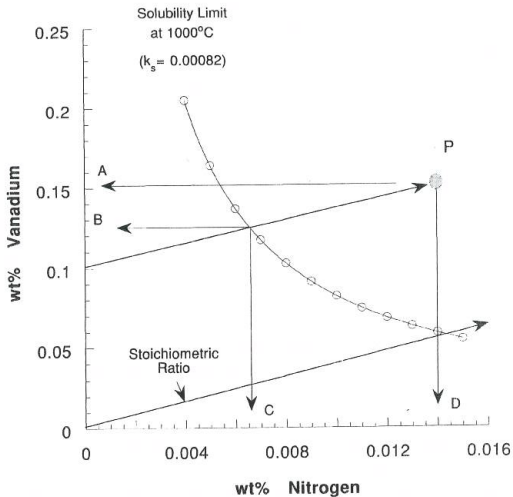
$$N_T = [N] + N_{VN}$$

$$N_{VN} = V_{VN} \frac{A_N}{A_V}$$

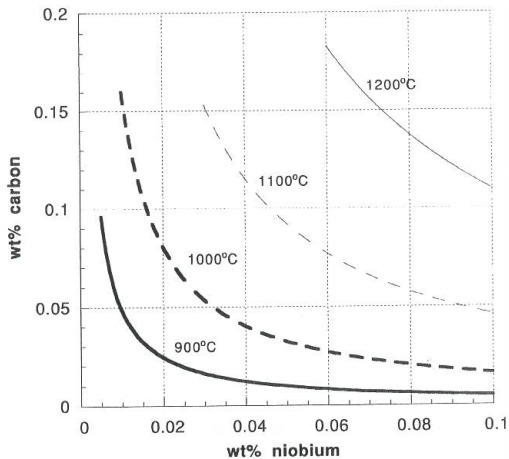
$$k_s = [V][N]$$

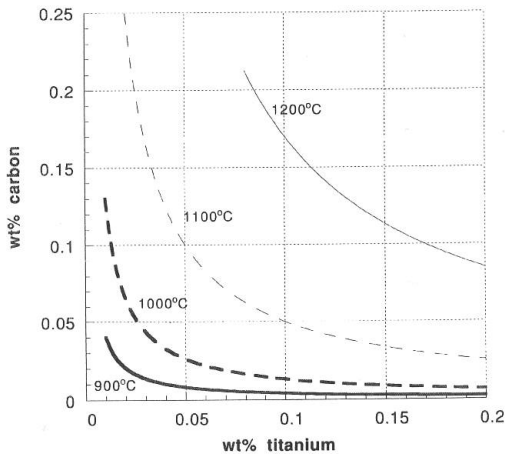
$$\begin{aligned}k_s &= [V][N] \\&= (V_T - V_{VN})(N_T - N_{VN}) \\&= (V_T - V_{VN}) \left(N_T - V_{VN} \frac{A_N}{A_V} \right)\end{aligned}$$

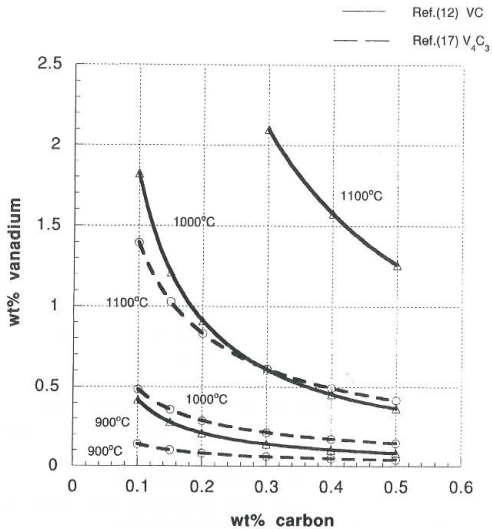
$$\begin{aligned}V_{VN} &= \frac{1}{2} \frac{A_V}{A_N} \left[\left(N_T + V_T \frac{A_N}{A_V} \right) \right. \\&\quad \left. - \sqrt{\left(N_T + V_T \frac{A_N}{A_V} \right)^2 - 4 \frac{A_N}{A_V} (V_T N_T - k_s)} \right]\end{aligned}$$

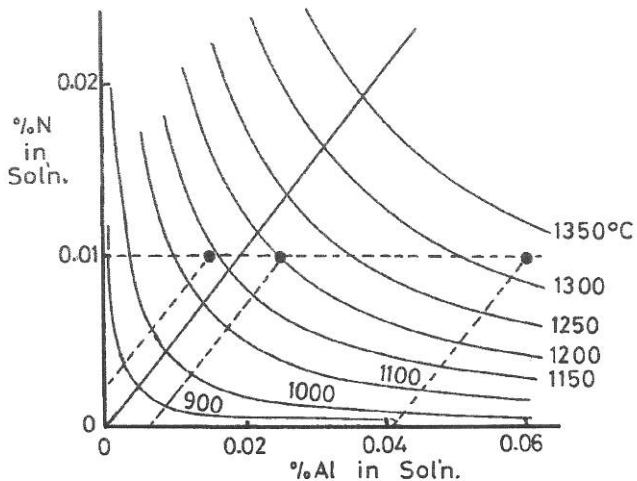


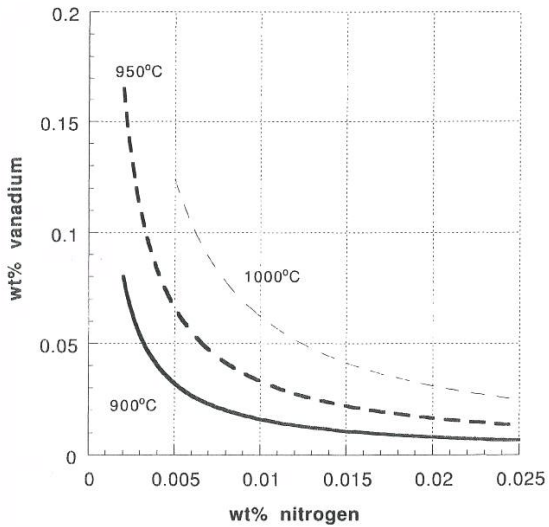
$$\frac{A - B}{D - C} = \frac{51}{14}$$

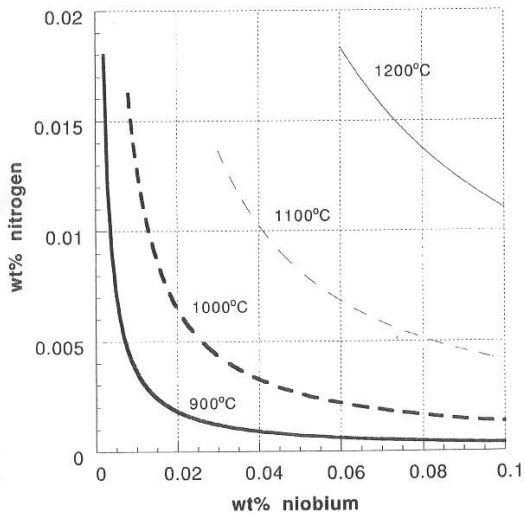


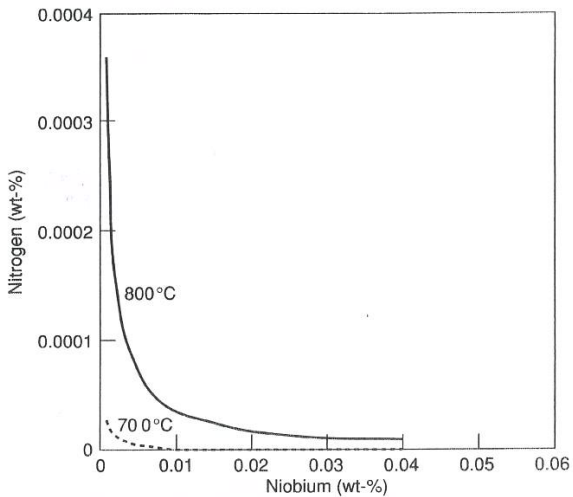












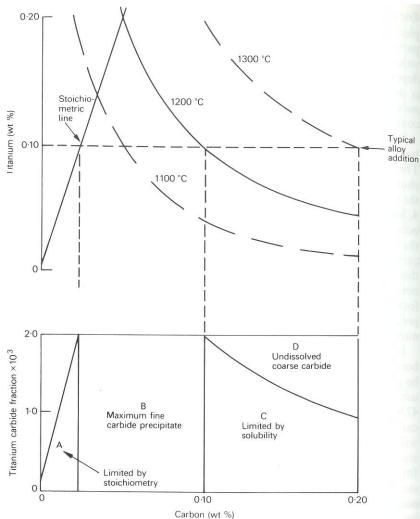


Fig. 9.7 Effect of stoichiometry on the precipitation of TiC in a micro-alloyed steel (Gladman *et al.*, In: *Micro-alloying 75*, Union Carbide Corporation, 1975)

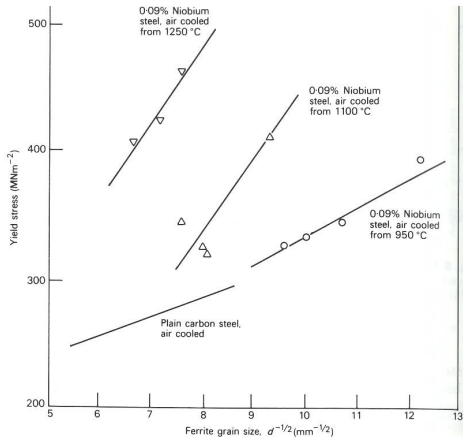


Fig. 9.6 Effect of austenizing temperature on the yield strength of a 0.1C-0.6Mn-0.09Nb steel (Gladman *et al.*, In: *Micro-alloying 75*, Union Carbide Corporation, 1975)

Precipitation of carbides, nitrides and carbonitrides

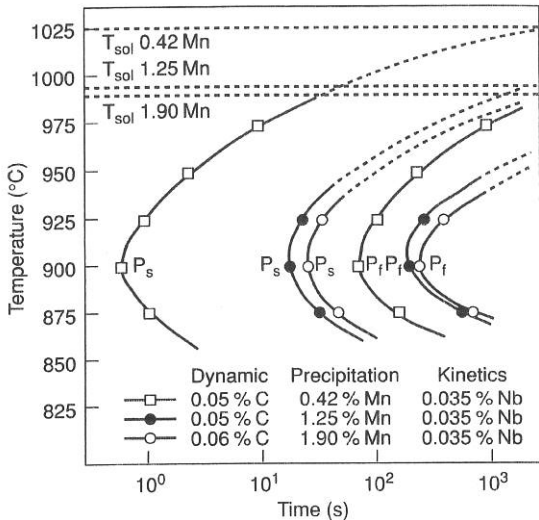
Precipitation in austenite

Precipitation during the $\gamma \rightarrow \alpha$ transformation

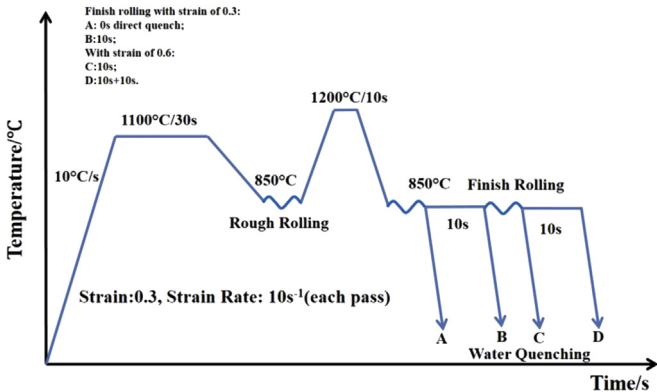
Continuous growth of carbide fibres or laths

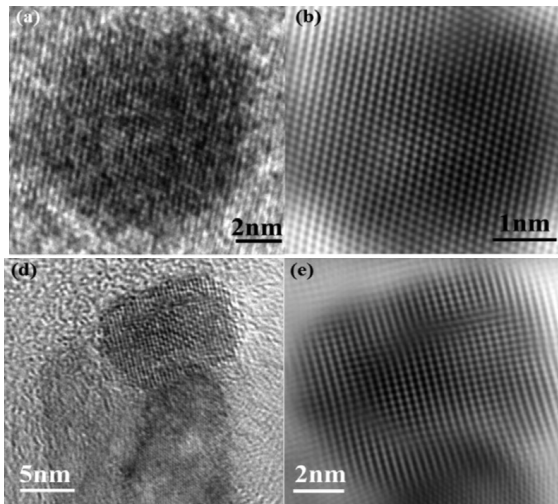
Interphase precipitation

Precipitation in ferrite



	C	Si	Mn	Cr	Ni	Nb	Ti	N	P
Nb steel	0.067	0.11	0.77	0.01	0.02	0.03	<0.01	0.0058	0.016
Nb-Ti steel	0.065	0.11	0.77	0.01	0.02	0.03	0.02	0.0062	0.016





Continuous growth of carbide fibres or laths

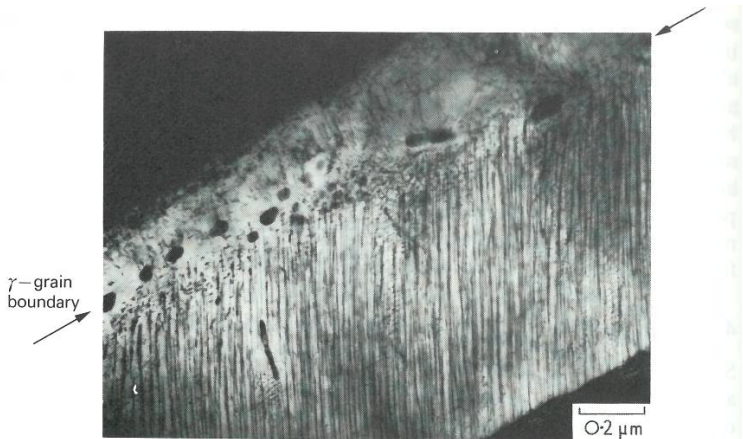
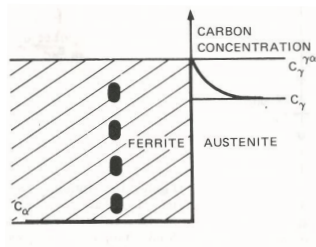
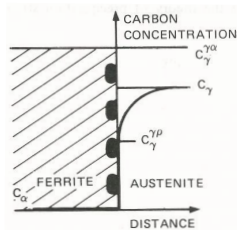
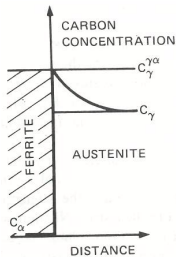


Fig. 4.13 Fe-4Mo-0.2C transformed 20 min at 650°C. Fibrous Mo_2C growth from γ boundary (Berry). Thin-foil EM

Interphase precipitation



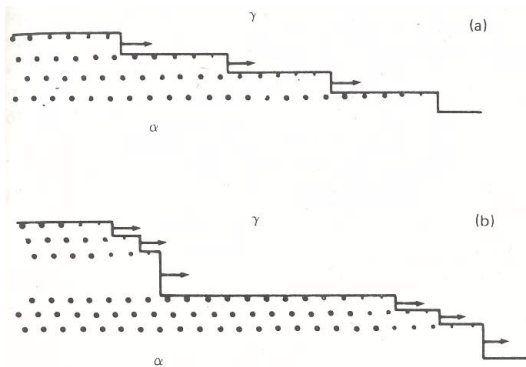


Figure VI-7. The mechanism of nucleation and growth of carbides on the γ - α interface. (R.W.K. Honeycombe, *Met. Trans. A*, 7A:915 (1976), by permission.)

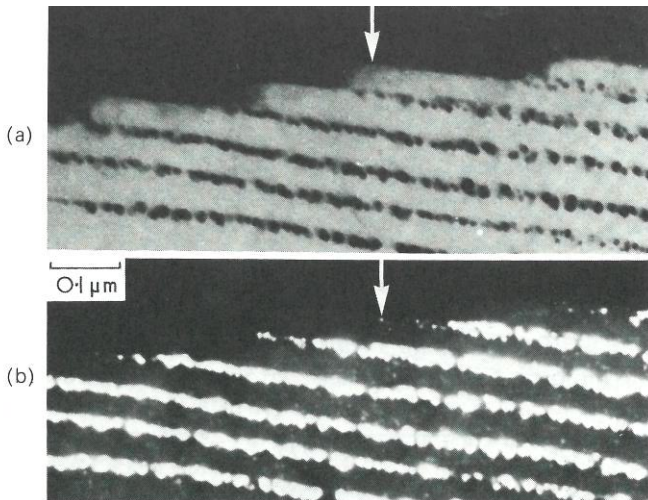


Fig. 4.16 Fe-12Cr-0.2C transformed 30 min at 650°C. Precipitation of $M_{23}C_6$ at stepped γ/α interface: a, bright field; b, precipitate spot dark field (Campbell). Thin-foil EM



Fig. 5.5 Vanadium carbo-nitride particles having the interphase precipitate morphology and distribution in the interlamellar ferrite of the pearlite eutectoid structure (dark field transmission electron micrograph).

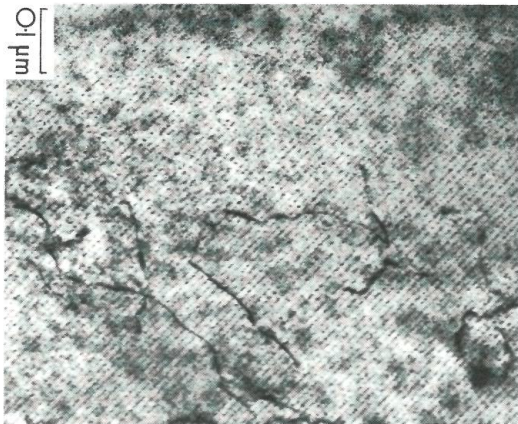
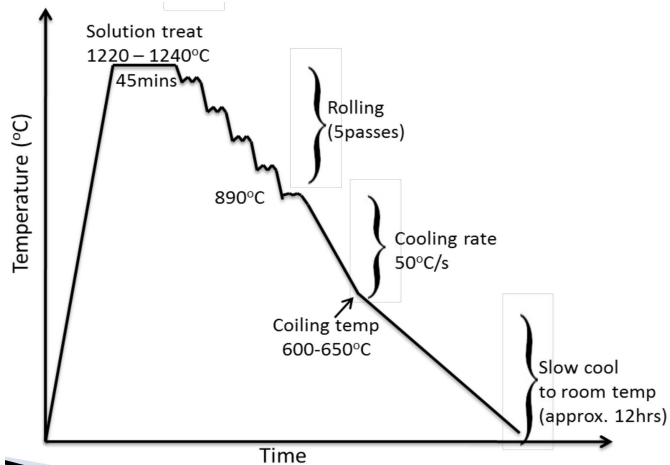


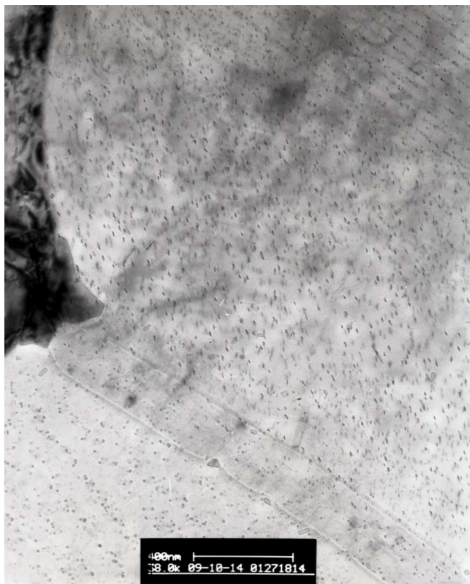
Fig. 4.14 Fe-0.75V-0.15C transformed 5 min at 725°C. Interphase precipitation of VC in ferrite

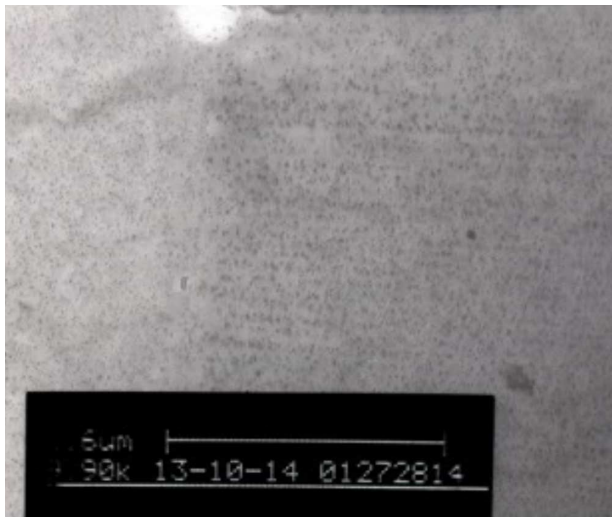
Model carbide precipitation hardened steel: 630VMoNb

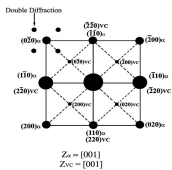
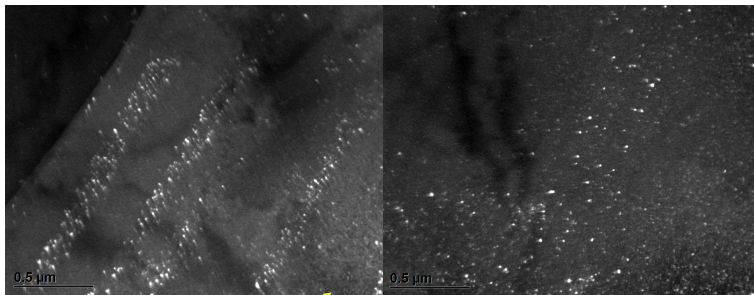
0.096C–1.6Mn–0.51Mo–0.26Si–0.25V–0.05Al–0.056Nb

$\sigma_y=902$ MPa; U.T.S.=964 MPa; elongation 18.2%



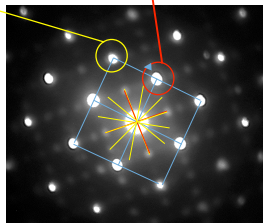


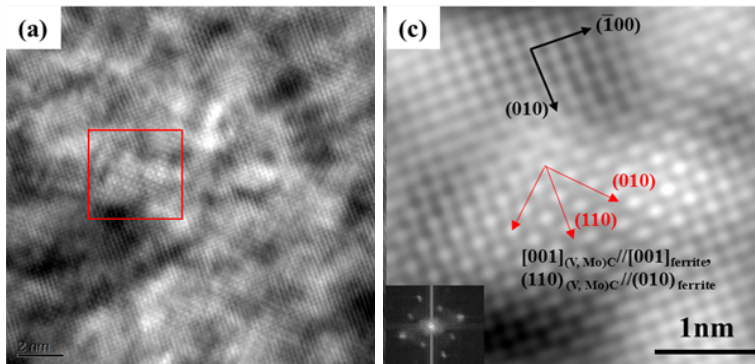




$$[100]_{(V, Mo)C} // [100]_{\alpha}$$

$$(200)_{(V, Mo)C} // (110)_{\alpha}$$





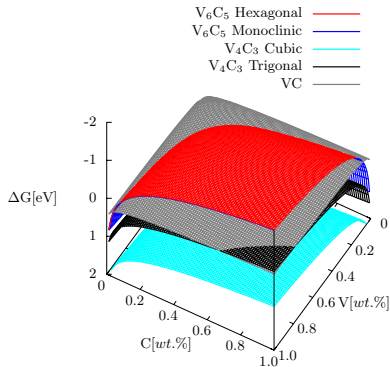


FIG. 5. Gibbs free energy –at a Temperature of 800 °C– for each of the studied compounds as a function of the content of C and V.

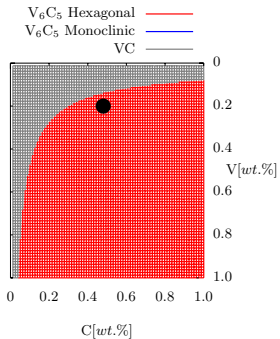
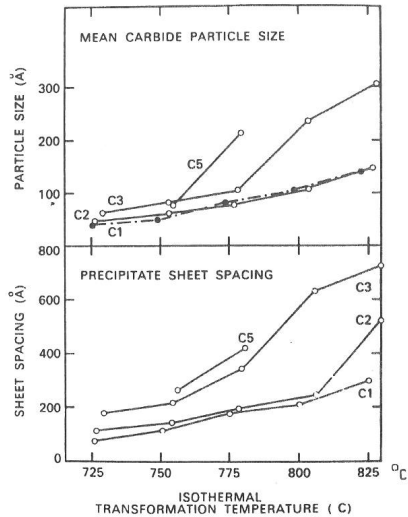


FIG. 6. Alternative top view of Figure 5 showing only the structures with the lowest Gibbs energies. The black dot indicates the composition of the steel from reference [6].



Precipitation in ferrite—age hardening

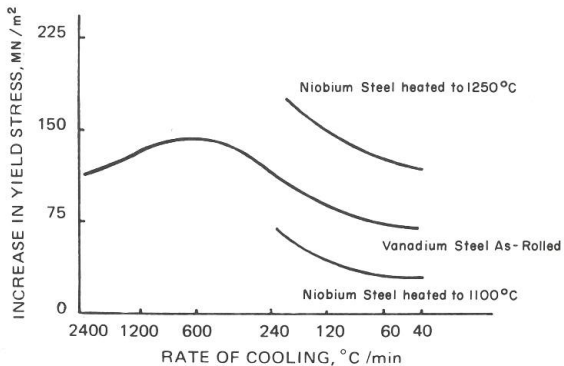
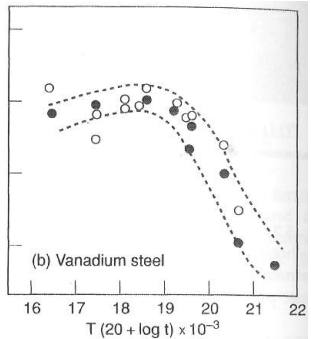
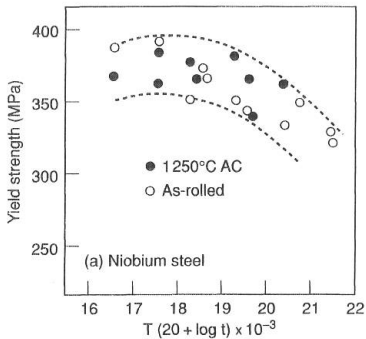
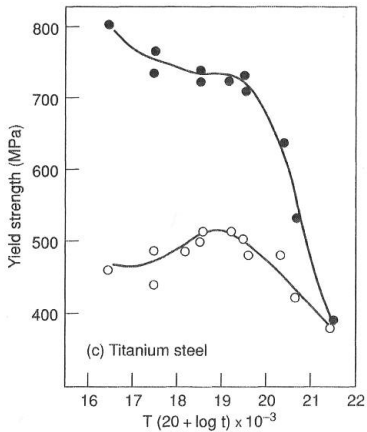


Fig. 4.5. *Effect of rate of cooling on the strengthening due to precipitated carbides in niobium and vanadium steels.*





	α'	α_{LB}	α_{UB}	α_a	α_W	α	α_i	P
Nucleation and growth reaction	Y	Y	Y	Y	Y	Y	Y	Y
Plate morphology	Y	Y	Y	Y	Y	N	N	N
IPS shape change with shear component	Y	Y	Y	Y	Y	N	N	N
Diffusionless nucleation	Y	N	N	N	N	N	N	N
Only carbon diffuses during nucleation	N	Y	Y	Y	Y	N	N	N
Reconstructive diffusion during nucleation	N	N	N	N	N	Y	Y	Y
Often nucleates intragranularly on defects	Y	N	N	Y	N	N	Y	Y
Diffusionless growth	Y	Y	Y	Y	N	N	N	N
Reconstructive diffusion during growth	N	N	N	N	N	Y	Y	Y
All atomic correspondence during growth	Y	Y	Y	Y	N	N	N	N
Substitutional atomic correspondence during growth	Y	Y	Y	Y	Y	N	N	N
Bulk redistribution of substitutional atoms during growth	N	N	N	N	N	S	S	S
Local equilibrium at interface during growth	N	N	N	N	N	S	S	S
Local para-equilibrium at interface during growth	N	N	N	N	Y	S	S	N
Diffusion of carbon during transformation	N	N	N	N	Y	Y	Y	Y
Carbon diffusion-controlled growth	N	N	N	N	Y	S	S	S
Cooperative growth of ferrite and cementite	N	N	N	N	N	N	N	Y
High dislocation density	Y	Y	Y	Y	S	N	N	N
Incomplete reaction phenomenon	N	Y	Y	Y	N	N	N	N
Necessarily has a glissile interface	Y	Y	Y	Y	Y	N	N	N
Always has an orientation within the Bain region [†]	Y	Y	Y	Y	Y	N	N	N
Grows across austenite grain boundaries	N	N	N	N	N	Y	Y	Y
High interface mobility at low temperatures	Y	Y	Y	Y	Y	N	N	N
Displacive transformation mechanism	Y	Y	Y	Y	Y	N	N	N
Reconstructive transformation mechanism	N	N	N	N	N	Y	Y	Y

[†] "... a reproducible relation which may be irrational but is close to the rational N-W or K-S relation."

martensite: α' ; lower, upper bainite: α_{LB} , α_{UB} ; acicular, idiomorphic ferrite: α_a , α_i ;

Widmanstätten ferrite: α_W ; allotriomorphic and massive ferrite: α ; pearlite: P

Y: yes; N: no; S: sometimes

After H. K. D. H. Bhadeshia and J. W. Christian

Principal features of martensite in steel

Mechanical properties

Transformation at constant composition

Athermal

Shape change: hence strain energy

Irrational habit planes

Crystallographic orientation relation

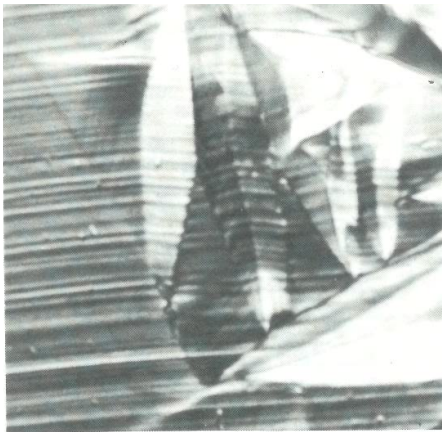


Fig. 5.3 Fe-30.5Ni-0.3C, illustrating the displacement of surface scratches by the martensitic shear (Bhadeshia). Nomanski interference contrast, $\times 650$

Kurdjumov–Sachs (K–S)

$$(111)_\gamma \parallel (101)_\alpha$$

$$[\bar{1}\bar{1}0]_\gamma \parallel [11\bar{1}]_\alpha$$

Nishiyama–Wasserman (N–W)

$$(111)_\gamma \parallel (110)_\alpha$$

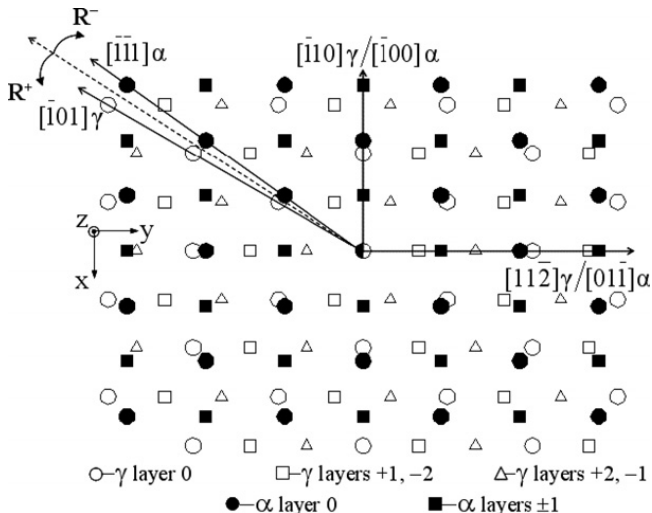
$$[\bar{1}10]_\gamma \parallel [001]_\alpha$$

$$[11\bar{2}]_\gamma \parallel [\bar{1}10]_\alpha$$

Greninger–Troiano (G–T)

$$(111)_\gamma \parallel (110)_\alpha$$

$$[\bar{1}2\ 17\ \bar{5}]_\gamma \parallel [\bar{1}7\ 17\ 7]_\alpha \text{ or } [\bar{1}2\bar{1}]_\gamma \text{ } 1^\circ \text{ away from } [1\bar{1}0]_\alpha$$



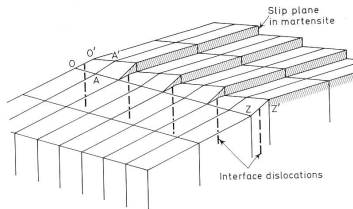


FIG. 5.2 The formation of single crystal martensite (schematic). OA and $O'A'$ are corresponding lattice vectors. OZ and $O'Z'$ are identical habit plane vectors.

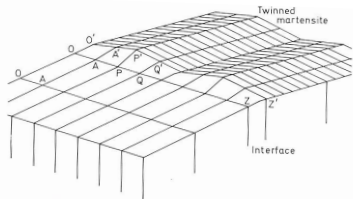
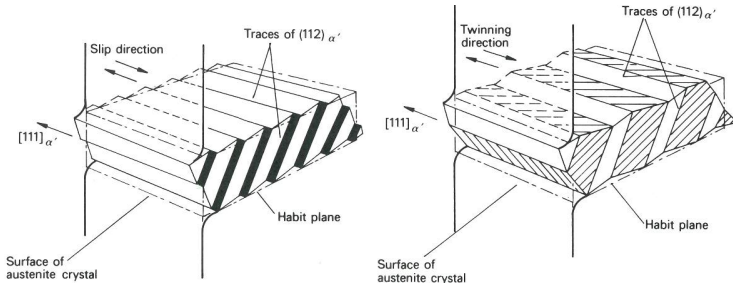
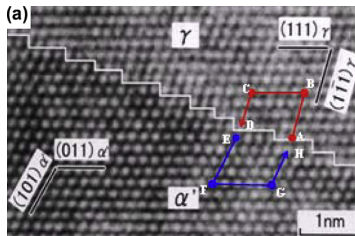
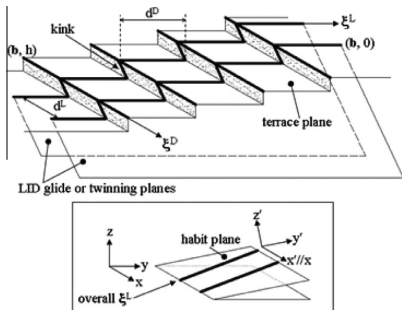


FIG. 5.1 The formation of twinned martensite (schematic). OA and $O'A'$ are corresponding lattice vectors in the parent and one product orientation; PQ and $P'Q'$ are corresponding vectors in the parent and the other product orientation. Macroscopic habit plane vectors OZ become identical vectors $O'Z'$.



Glissile interface



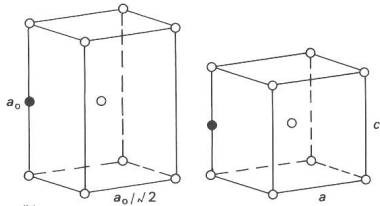
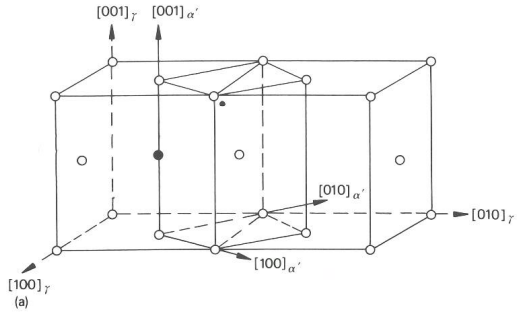
TEM lattice image of Fe-20.2%Ni-5.4%Mn γ - α' interface. Terraces are $(111)_\gamma$ and habit plane is approximately $(121)_\gamma$.

Phenomenological Theory of Martensite

Lattice correspondence (Bain)

Lattice rotation

Lattice invariant strain (slip and / or twinning)



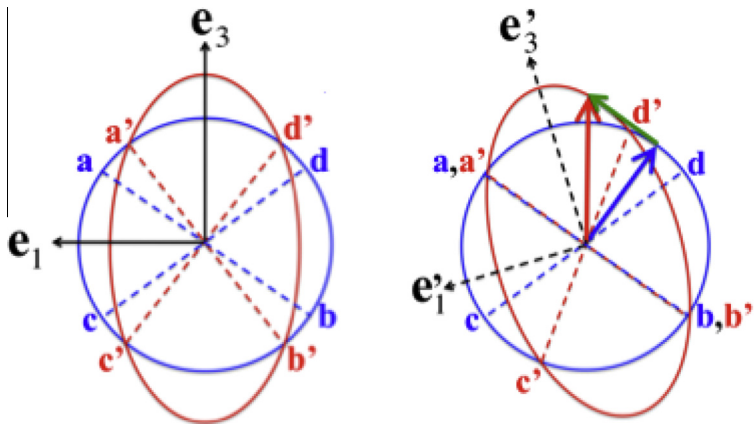
$$\mathbf{B} = \begin{pmatrix} \epsilon_0 & 0 & 0 \\ 0 & \epsilon_0 & 0 \\ 0 & 0 & \epsilon'_0 \end{pmatrix}$$

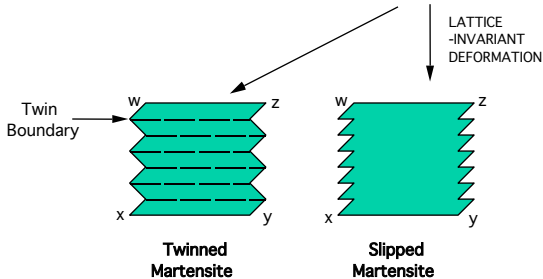
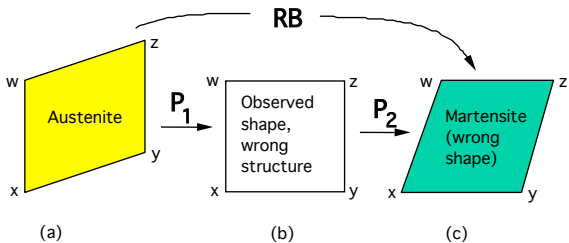
$$\epsilon_0 = \frac{\sqrt{2}a_{\alpha'} - a_{\gamma}}{a_{\gamma}} \quad ; \quad \epsilon'_0 = \frac{a_{\alpha'} - a_{\gamma}}{a_{\gamma}}$$

\mathbf{B} = Bain strain

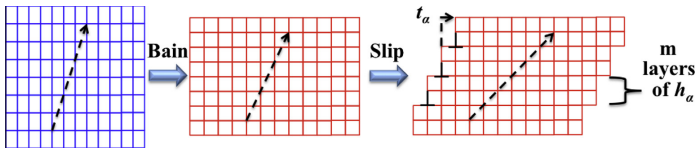
\mathbf{R} = rotation

$$\mathbf{P}_2\mathbf{P}_1 = \mathbf{R}\mathbf{B}$$

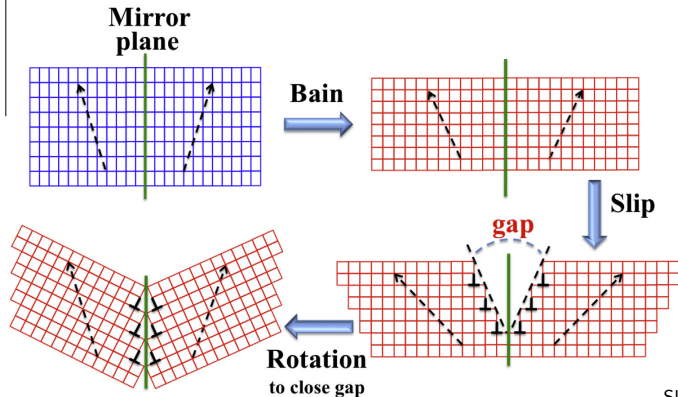


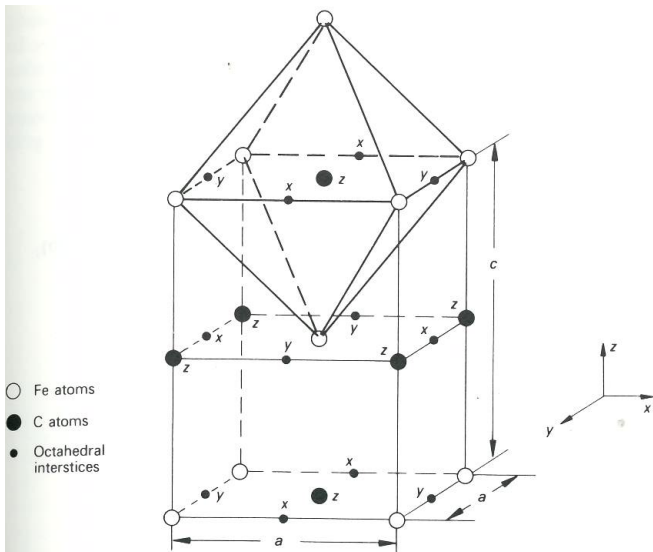


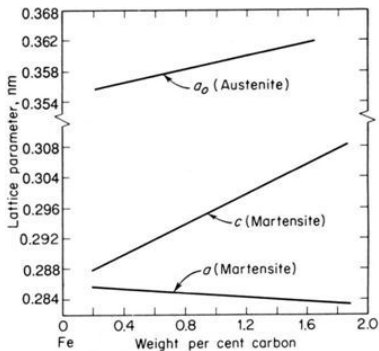
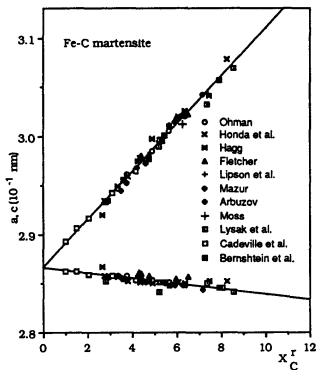
Correct macroscopic shape, correct structure



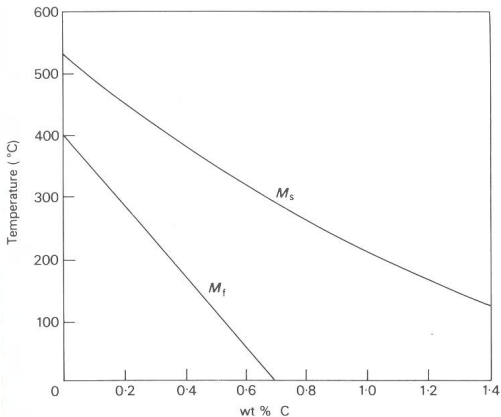
(a)



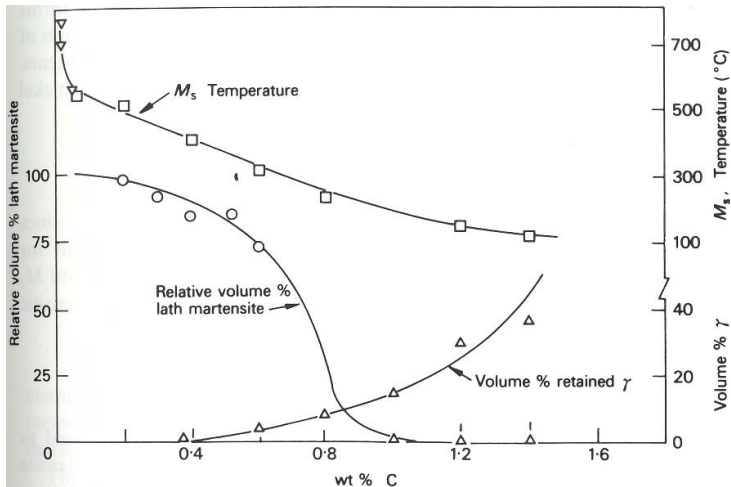




Steel martensite is tetragonal !



$$M_s(^{\circ}\text{C}) = 539 - 423 \times \%C - 30.4 \times \%Mn - 17.7 \times \%Ni - 7.5 \times \%Mo$$



Low carbon martensite up to 0.6wt% C, and Fe–Ni–Mn alloys

Habit planes : $\{557\}_\gamma$ (three variants to each $\{111\}_\gamma$ plane)

Orientation relation: **K–S**

Lath martensite

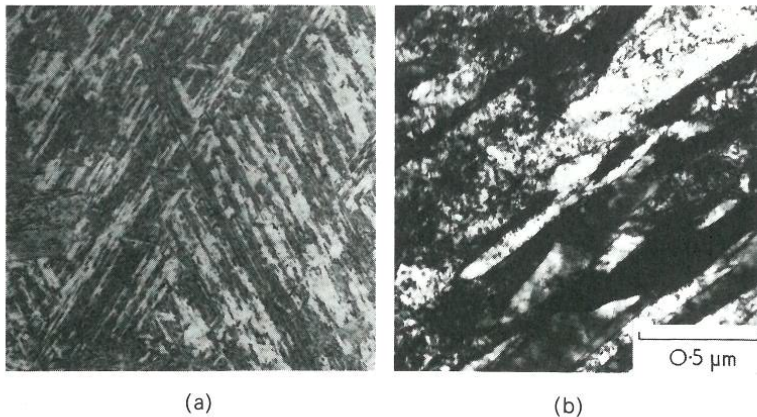
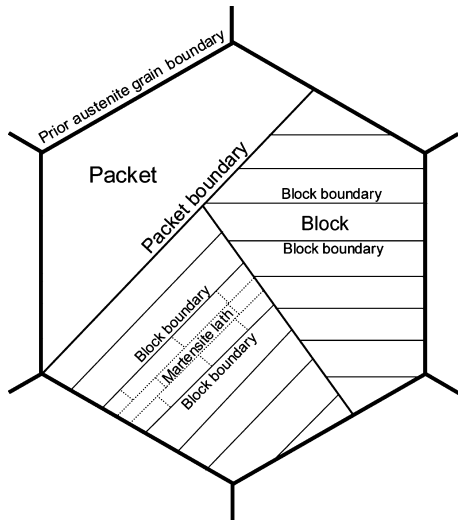
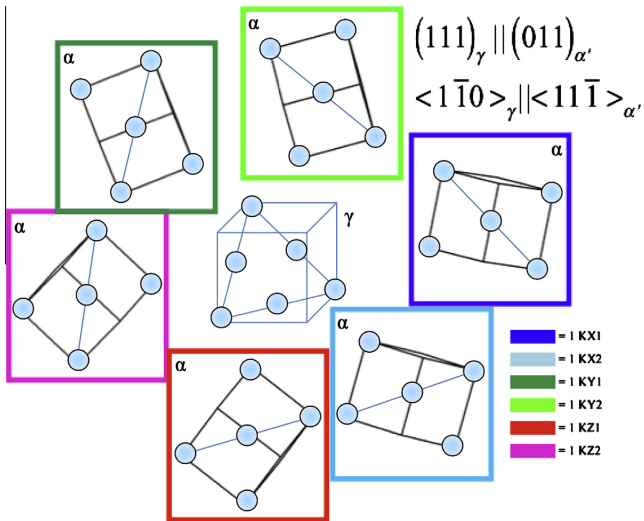
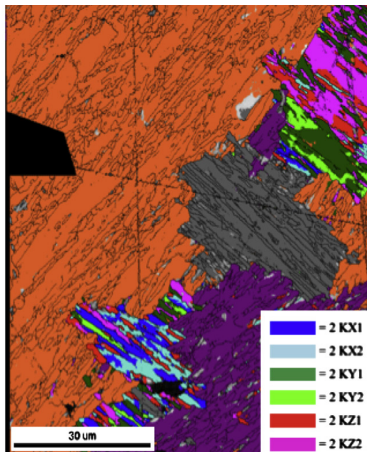
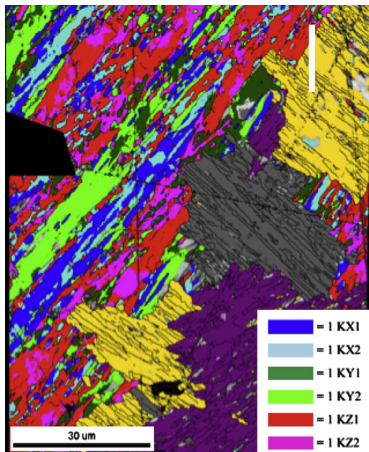


Fig. 5.10 Fe-0.16C alloy. Martensite formed by quenching from 1050°C: a, optical micrograph, $\times 95$; b, thin-foil EM showing heavily dislocated laths (Ohmori)





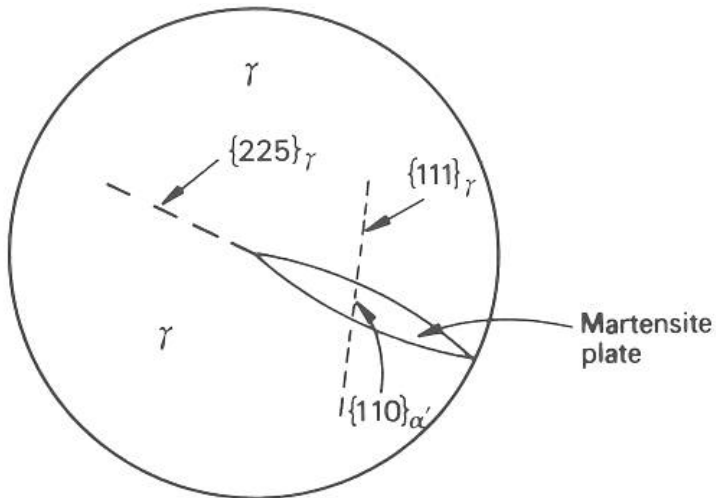


Medium carbon martensite 0.5–1wt% C

Habit plane : $\{225\}_{\gamma}$

Orientation relation: **K–S**

“acicular” martensite



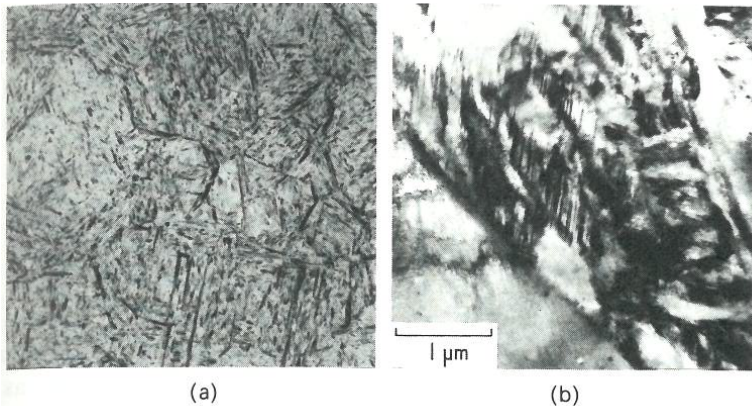


Fig. 5.11 Fe-0.8C alloy quenched from 1100°C: a, optical micrograph $\times 200$; b, thin-foil EM showing twinning in martensite laths (Ohmori)

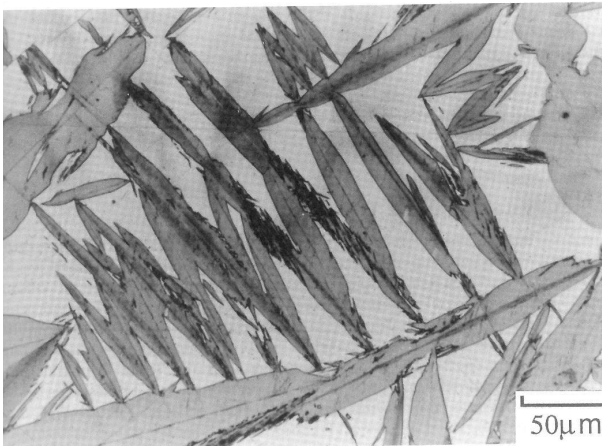
High carbon martensite more than 1wt% C, and high Ni steels

Habit plane : $\{259\}_{\gamma}$

Orientation relation: **N-W**

Plate martensite

Bursts

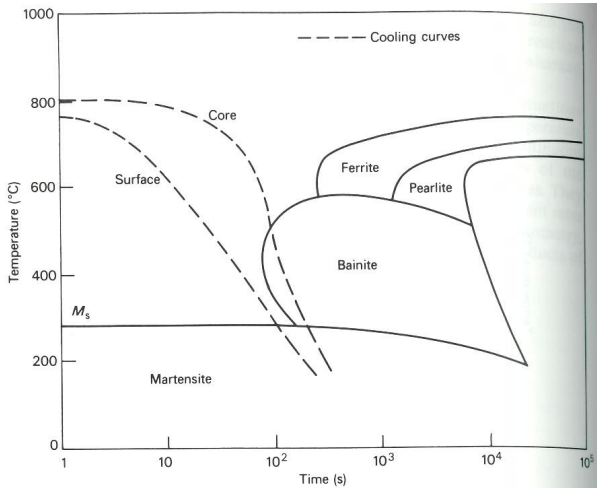


Burst martensite in Fe-30%Ni-0.31%C



Fig. 5.7 Fe-1.8C-3Mn-2Si. Lenticular martensite illustrating the burst phenomenon (Bhadeshia). Optical micrograph, $\times 300$

Hardenability



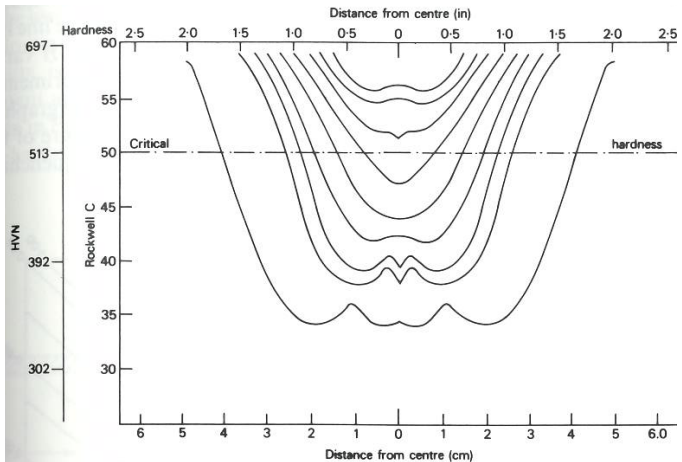


Fig. 7.3 1.1 Ni-0.75Cr-0.4C steel. Hardness data from transverse sections through water-quenched bars of increasing diameter (Grossman *et al.*, In:

Cooling stages

1. Vapour blanket

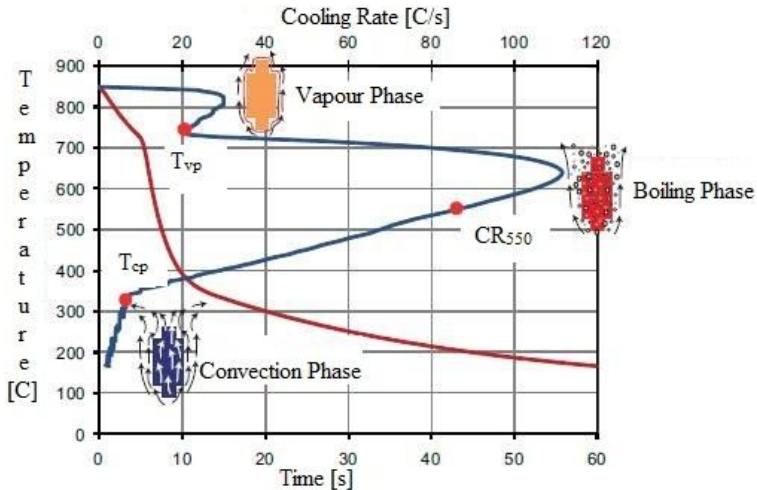
Cooling by radiation, depending on *emissivity* of the steel

2. Nucleate boiling

Quench medium boils

3. Convective cooling

Specimen fully covered by quenchant



In one dimension, Fourier's law is

$$q = -k \frac{\partial T}{\partial x} \quad [\text{J s}^{-1} \text{m}^{-2}]$$

The heat conduction equation is

$$\frac{\partial T}{\partial t} = \kappa \frac{\partial^2 T}{\partial x^2}$$

Newton's law of cooling is

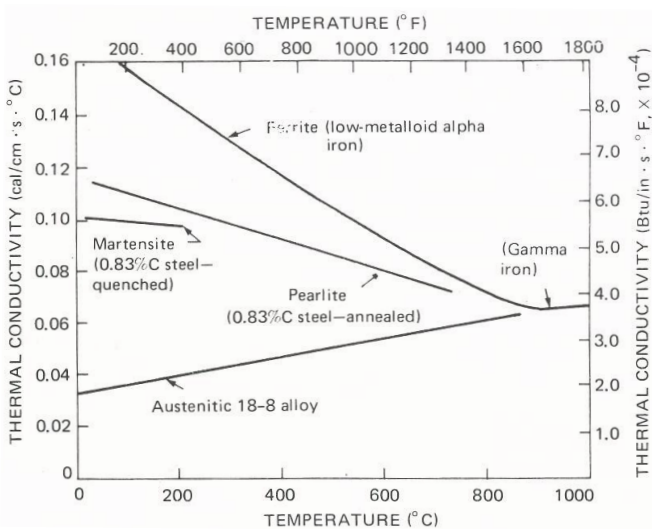
$$q = h(T_1 - T_2) = h(\text{temperature of body} - \text{temperature of surroundings})$$

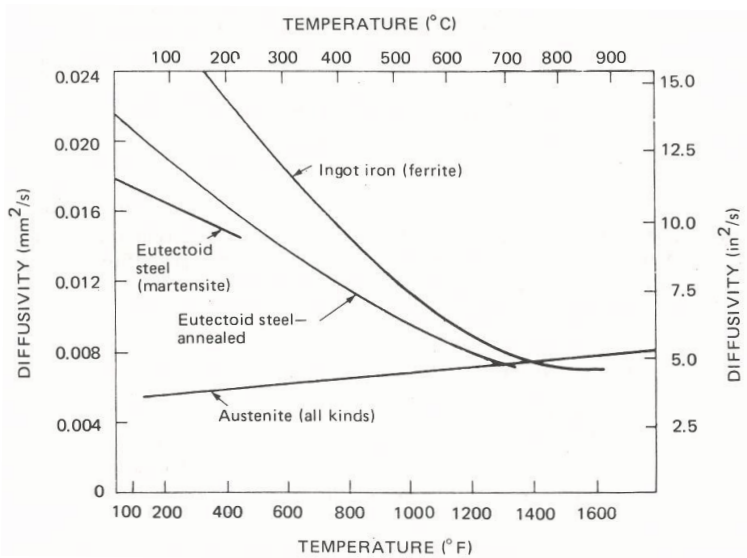
$$k(T) = \text{thermal conductivity} [\text{J s}^{-1} \text{m}^{-1} \text{K}^{-1}]$$

$$\kappa(T) = \frac{\text{thermal conductivity}}{\text{volume heat capacity}} = \text{thermal diffusivity} [\text{m}^2 \text{s}^{-1}]$$

$$h(T) = \text{heat transfer coefficient} [\text{J s}^{-1} \text{m}^{-2} \text{K}^{-1}]$$

$$H(T) = \text{quench severity} [\text{m}^{-1}] = \frac{h}{2k} \propto \text{Biot number} \times \frac{\text{area}}{\text{volume}}$$





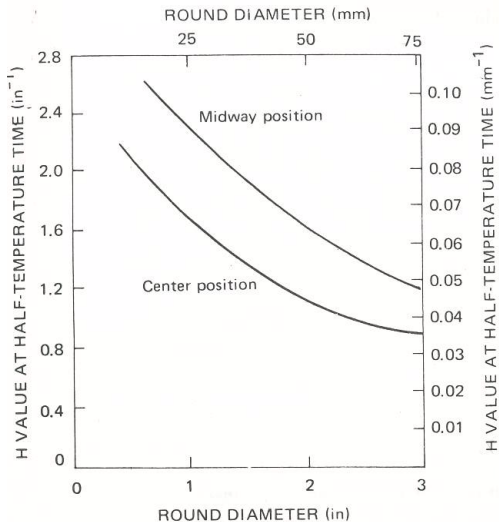


Figure VII-25. Variation of H value at half-temperature time in round bars water-quenched from 845°C . (D.J. Carney, *Trans. Am. Soc. Met.*, 46:882 (1954), by permission.)

Table VII-5 Approximate values of H (severity of quench)¹

Agitation	Oil	Water	Brine
None	0.25-0.30	0.9-1.0	2
Mild	0.30-0.35	1.0-1.1	2.0-2.2
Moderate	0.35-0.40	1.2-1.3	
Good	0.40-0.50	1.4-1.5	
Strong	0.50-0.80	1.6-2.0	
Violent	0.80-1.1	4.0	5.0

¹ H.E. McGannon, ed., *Making, Shaping and Treating of Steel*, U.S. Steel Corp., Pittsburgh, 1971, p. 1099.

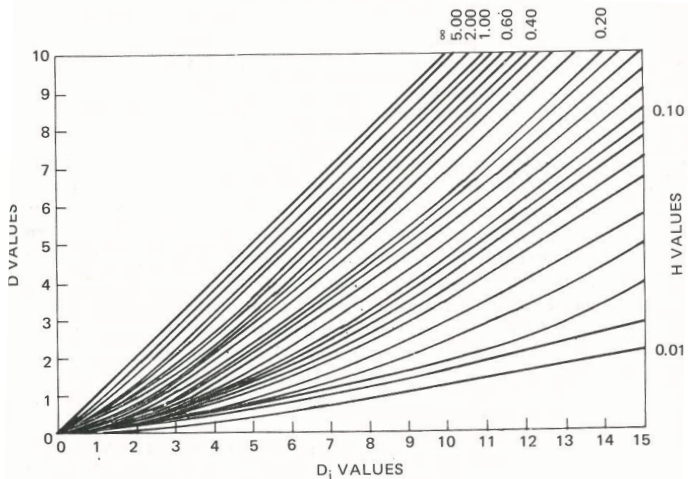


Figure VII-26. Relationships among ideal diameter, critical diameter, and severity of quen (*Making, Shaping and Treating of Steel*, 9th ed., 1971, copyright United States Steel Corporation)

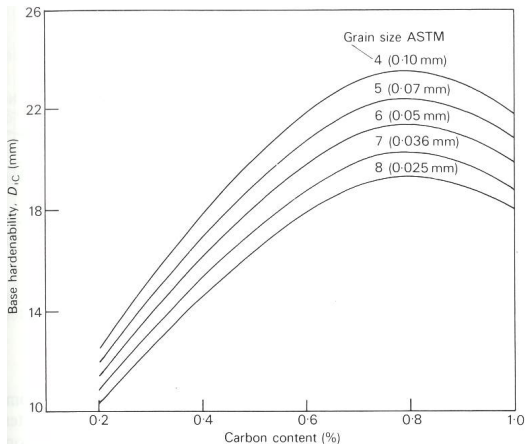
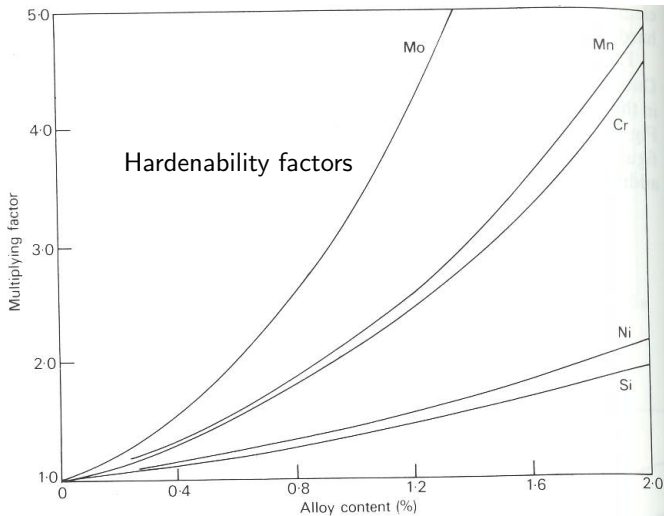


Fig. 7.9 Effect of carbon content and grain size on base hardenability (Moser and Legat, *Härtereitechn. Mitt.*, 1969, **24**, 100)



The two principal variables that influence hardenability of steel are:

1. prior austenite grain size
2. composition

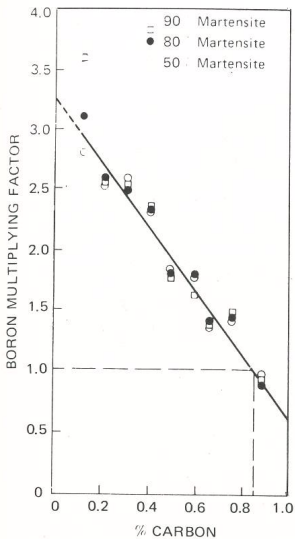


Figure VII-50. Effect of carbon on boron multiplying factor in 0.8%Mn steels. (D.T. Llewellyn and W.T. Cook, *Met. Technol.*, 1:517 (1974), by permission.)

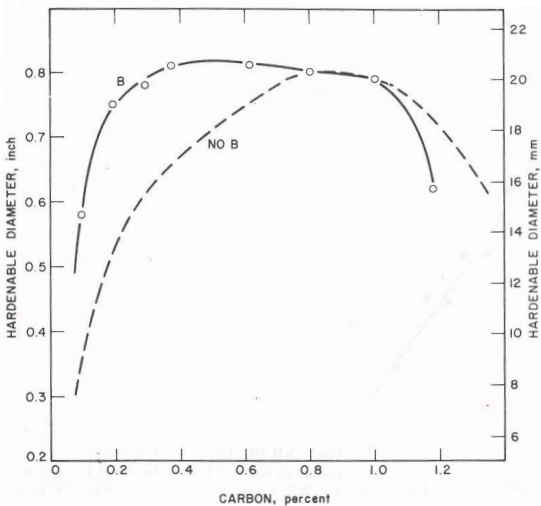


Figure VII-51. Hardenable diameter (90% martensite at center of Fe-0.5%Mn alloys, as-water-quenched, with and without boron at an austenite grain size of ASTM 4). (R.A. Grange and C.R. Hribal, U.S. Steel Corporation Tech. Rept 40.061 (1), June 1972, by permission.)

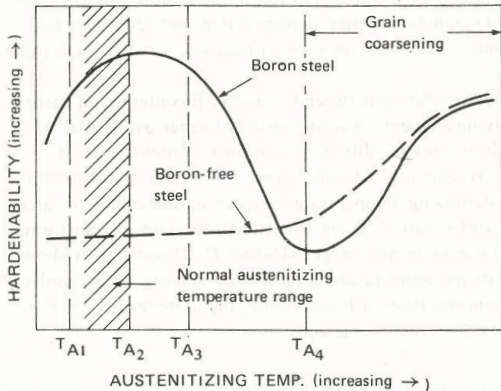


Figure VII-52. Schematic representation of effect of austenitizing temperature in a boron steel and a corresponding boron-free steel. (R.A. Grange and J.B. Mitchell, *Trans. Am. Soc. Met.*, 53:157 (1961).)

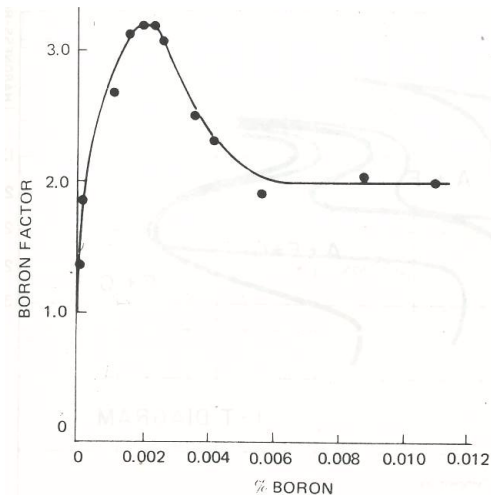
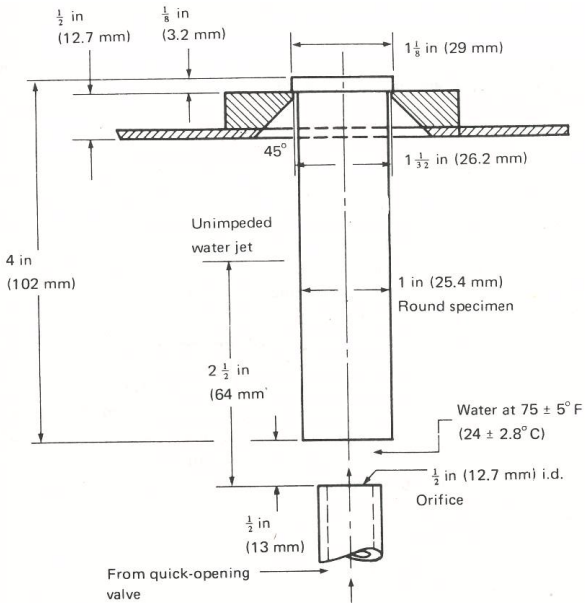
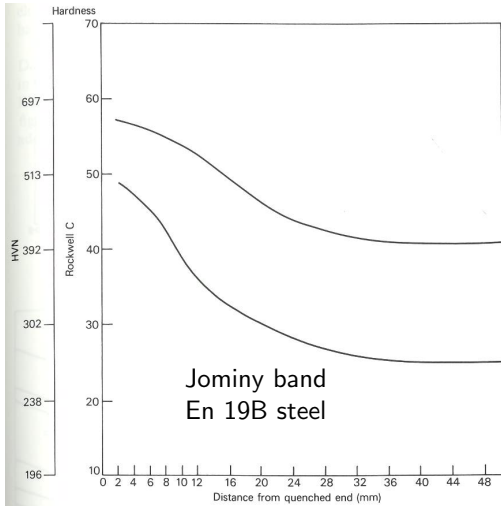


Figure VII-53. Boron hardenability factors as a function of boron content in a 0.20%C-0.55%Mo steel. (G.F. Melloy, P.R. Slimmon, and P.P. Podgurski, *Met. Trans.*, 4:2279 (1973), by permission.)





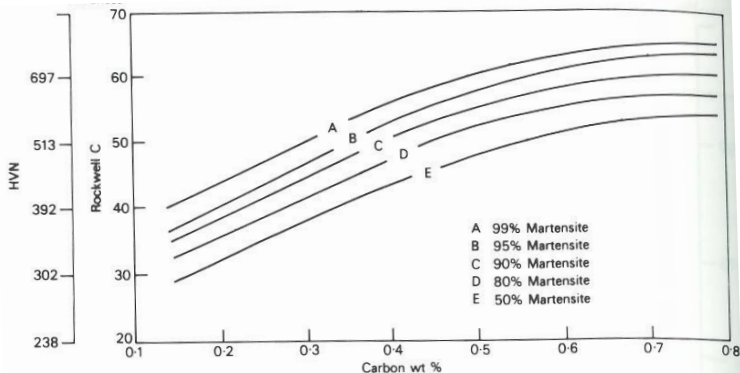


Fig. 7.7 The effect of % martensite and carbon content on as-quenched hardness (Hodge and Orohoski, In: Thelning, *Steel and its Heat Treatment*, Bofors Handbook, Butterworths, 1975)

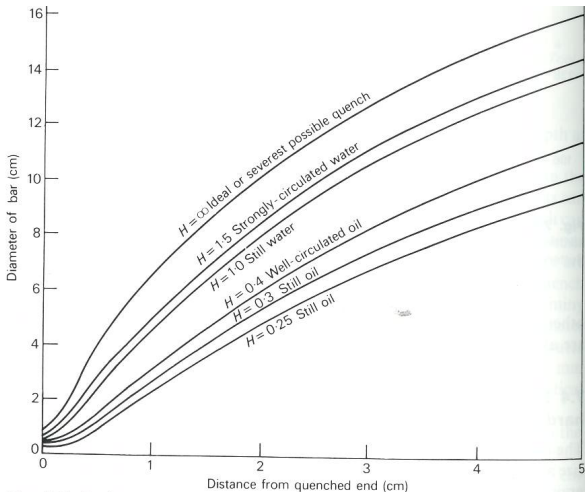


Fig. 7.8 Equivalent Jominy positions and bar diameter, where the cooling rate for the bar centre is the same as that for the point in the Jominy specimen. Curves are plotted for a range of cooling rates (Grossman and Bain, *Principles of Heat Treatment*, ASM, 1964)

Tempering

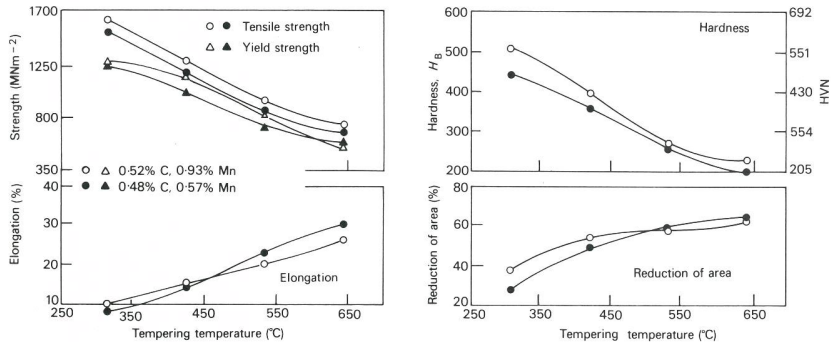


Fig. 8.7 Properties of water-quenched and tempered 1050 steel (C 0.48–0.55, Mn 0.6–1.07) (Metals Handbook, 8th edition, Volume 1, ASM)

Stage 1: up to 250°C; precipitation of $\epsilon\text{-Fe}_3\text{C}$, partial loss of tetragonality.

Stage 2: 230–300°C; decomposition of retained austenite.

Stage 3: 200–350°C; $\epsilon\text{-Fe}_3\text{C}$ transforms to $\theta\text{-Fe}_3\text{C}$ (cementite), loss of tetragonality.

Stage 4: >350°C; θ coarsens and spheroidises, ferrite recrystallises.

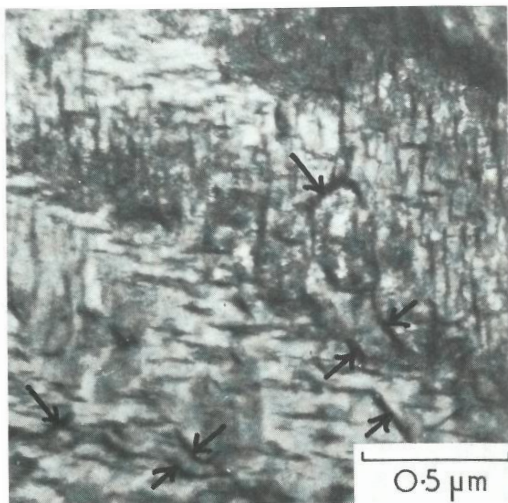


Fig. 8.2 Fe-0.8C quenched and tempered at 250°C. Precipitates of ϵ carbide and cementite (arrowed) (Ohmori). Thin-foil EM

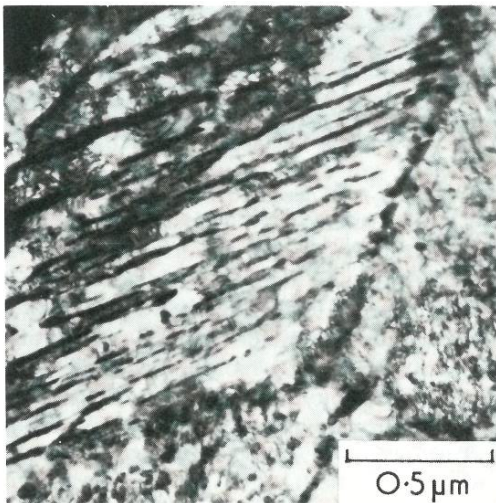


Fig. 8.3 Fe-0.8C quenched and tempered at 450°C. Fe₃C growing along twin boundaries (Ohmori). Thin-foil EM

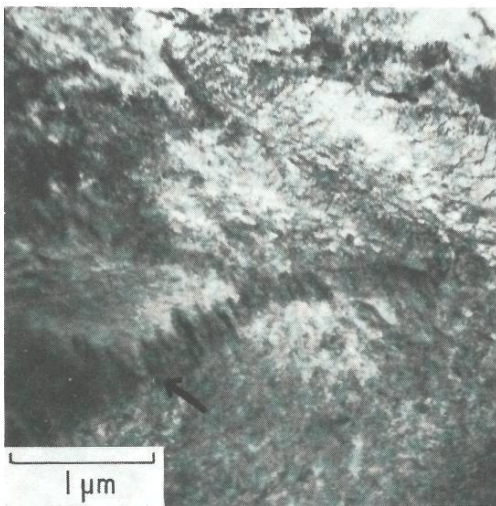


Fig. 8.4 Fe-0.8C quenched and tempered at 250°C. Grain boundary precipitation of cementite (Ohmori). Thin-foil EM

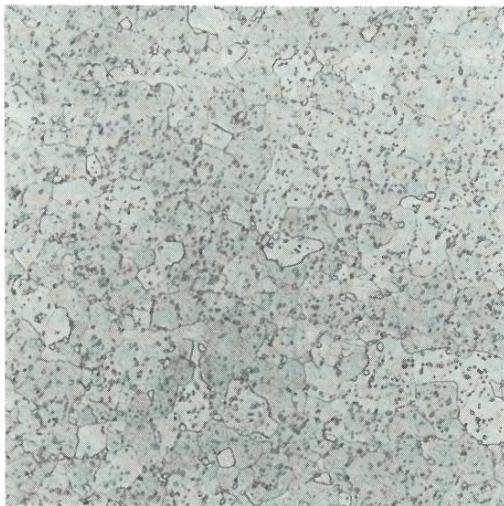


Fig. 8.5 Fe-0.17C water quenched from 900°C and tempered 5h at 650°C. Spheroidized Fe₃C in equi-axed ferrite (lens). Optical micrograph, ×350

